Structure and mechanotransmission mechanism of the MacB ABC transporter superfamily

Allister Crow, Nicholas P. Greene*, Elise Kaplan, Vassilis Koronakis*
**Joint first authorship*

Department of Pathology, University of Cambridge, Tennis Court Road, Cambridge, CB2 1QP, United Kingdom.

ABSTRACT

MacB is an ABC transporter that collaborates with the MacA adaptor protein and TolC exit duct to drive efflux of antibiotics and enterotoxin STII out of the bacterial cell. Here we present the structure of ATP-bound MacB and reveal precise molecular details of its mechanism. The MacB transmembrane domain lacks a central cavity through which substrates could be passed but instead conveys conformational changes from one side of the membrane to the other; a process we term mechanotransmission. Comparison of ATP-bound and nucleotide-free states reveals how reversible dimerization of the nucleotide binding domains drives opening and closing of the MacB periplasmic domains via concerted movements of the second transmembrane segment and major coupling helix. We propose the assembled tripartite pump acts as a molecular bellows to propel substrates through the TolC exit duct, driven by MacB mechanotransmission. Homologues of MacB that do not form tripartite pumps but share structural features underpinning mechanotransmission include the LolCDE lipoprotein trafficking complex and FtsEX cell division signaling protein. The MacB architecture serves as the blueprint for understanding the structure and mechanism of an entire ABC transporter superfamily and the many diverse functions it supports.

SIGNIFICANCE

Bacterial ABC transporters typically mediate transport of substrates across the cytoplasmic membrane using either alternating access or toppling based mechanisms. The non-canonical ABC transporter MacB does not behave in this manner, but instead couples cytoplasmic ATP hydrolysis with periplasmic conformational changes that drive substrates from the periplasm to the extracellular space via the TolC exit duct. Here we describe the 'mechanotransmission' mechanism of MacB in molecular detail by comparing ATP-bound and nucleotide-free structures. We further show that MacB shares its structural architecture with an entire superfamily of ABC transporters responsible for fundamental bacterial processes including cell division and outer membrane biogenesis suggesting a common mode of operation, and raise the possibility of targeting such proteins for development of new antibiotics.

\body

Tripartite efflux pumps (TEPs) span the inner and outer membranes of Gram-negative bacteria to mediate export of protein toxins, antibiotics and virulence factors (1). In *E. coli*, the inner membrane ABC transporter MacB (2), adaptor protein MacA and the TolC exit duct (3) form a TEP that confers resistance to macrolide antibiotics (2, 4, 5) and exports heat stable enterotoxin STII (6, 7). ABC transporters are composed of nucleotide binding domains (NBDs) required for ATP hydrolysis, and transmembrane domains (TMDs) that typically facilitate passage of the substrate through the membrane in which they reside using an alternating access or toppling mechanism (8, 9). MacB is unlikely to use such mechanisms for enterotoxin transport as it resides in the inner membrane and transports enterotoxin STII from the periplasm to the extracellular space (6).

MacB contains four transmembrane helices, an N-terminal NBD, and an extensive periplasmic domain located between TM1 and TM2 (10, 11). MacB homologues operate either within, or independently of, TEPs to perform a multitude of roles (12, 13). TEP-independent MacB homologues include key proteins involved in lipoprotein trafficking (LolCDE) and cell division (FtsEX) (12). LolCDE extracts lipoproteins from the inner membrane to a periplasmic chaperone (14) while FtsEX is thought to alter conformation of its periplasmic domain to recruit and activate periplasmic peptidoglycan hydrolases during bacterial cell division (15). Like MacB, LolCDE and FtsEX do not transport substrates across the inner membrane but instead use cytoplasmic ATP hydrolysis to perform work in the periplasm.

Here, we present the crystal structure of ATP-bound MacB at 3.35 Å that in combination with a nucleotide-free form derived from a cryoEM structure of the MacAB-TolC assembly (11) reveals a mechanotransmission mechanism. We demonstrate that MacB is representative of a wider family of ABC transporters that use the same architecture and mechanism to perform diverse biological functions.

RESULTS

The crystal structure of MacB defines a new ABC transporter fold. We determined structures of ATP-bound MacB using X-ray crystallography. After screening multiple MacB homologues, crystals of *Aggregatibacter actinomycetemcomitans* (hereafter *Aa*) MacB were obtained in two space groups, $P6_522$ and $P2_1$ and their structures solved at 3.90 Å and 3.35 Å resolution, respectively. Structures of the *E. coli* MacB periplasmic domain (1.95 Å) and cytoplasmic NBD (2.40 Å) were also determined. Structure determination for full-length *Aa*MacB was achieved using a combination of molecular replacement with the individual domains and selenomethionine-based anomalous scattering

approaches. X-ray data and refinement statistics are given in **Tables S1 & S2** and representative electron density for the full-length MacB structure is shown in **Movie 1**.

The structure of *Aa*MacB is shown in **Fig. 1a** coloured consistently with its linear domain arrangement (**Fig. 1b**) and transmembrane topology (**Fig. 1c**). Each MacB monomer within the dimer contains four transmembrane helices (TM1-4, *blue*), an N-terminal nucleotide-binding domain (NBD, *red*), and a 198-residue periplasmic domain (*purple*) located between TM1 and TM2. The periplasmic domain is itself made up of two subdomains; the Sabre (Small alpha/beta rich extracytoplasmic) subdomain is composed of a single contiguous region of the MacB polypeptide (residues 347-465) and the Porter is formed from two β-α-β motifs (306-346 and 466-503) located either side of the Sabre-encoding region. The entire periplasmic domain is elevated above the cytoplasmic membrane by a 4-helix bundle (**Fig. 1a**, *stalk*) comprising extensions of TM1 and TM2 from both monomers that interact along the dimer's symmetry axis. TM3 and TM4 are both shorter than TM1 and TM2 and are not involved in dimerization, packing on the outside of the 4-helix bundle. An 8-residue loop connects TM3 and TM4 on the periplasmic side straddling the interface between the outer leaflet of the cytoplasmic membrane and the periplasm (**Fig. 1a**, *shoulder*). On the cytoplasmic side of TM1, an 18-amino acid amphipathic helix (*teal,* 246-263) runs parallel with the plane of the membrane and is connected to the NBD by a 41-residue 'skirting loop' (*grey*, residues 224-264) that lacks secondary structure and is highly flexible. Residues 242-246 are too disordered to model. A short helix located between TM2 and TM3 forms the major coupling helix (*green*, residues 548-556) and an additional interaction with the NBD is made by the C-terminus (*minor coupling helix, orange,* residues 637-646).

The fold and topology of the MacB transmembrane and periplasmic domain are strikingly different to the six currently recognised ABC transporter superfamilies (**SI Appendix, Fig. S1**). The key distinguishing features of MacB are its four transmembrane helix topology, periplasmic domain, and stalk. MacB also has a rigid transmembrane dimerization interface dominated by hydrophobic interactions and lacks transmembrane cavities (**SI Appendix, Fig. S2**). The MacB structure supports previous bioinformatics-based analyses suggesting it belongs to a distinct monophyletic group with an independent evolutionary origin to all other ABC transporters that have been structurally characterised (12, 13). We therefore designate MacB as the 'type specimen' for a new ABC transporter superfamily on the basis of its novel topology, dimerization interface, and transmembrane fold - all of which are unique to MacB.

Mode of ATP-binding in MacB. The structures presented here represent ATP-bound conformations of MacB in which the two cytoplasmic ATP binding sites are each occupied by a single nucleotide. The locations of the ATP-binding sites are shown in **Fig. 1d** and an omit map showing unbiased electron density for one of the nucleotides appears in **Fig. 1e** and **Movie 2**. The ATP binding mode is

similar to that seen in other ABC transporters (8, 9), with the nucleotides sandwiched between dimerized NBDs. The ATP phosphates are co-ordinated by a bound magnesium ion and Lys46 (Lys47 in *E. coli*). The catalytic glutamate, Glu169 (Glu170 in *E. coli*, here mutated to glutamine), is positioned directly adjacent to the γ-phosphate consistent with a role in ATP hydrolysis. The MacB major coupling helix interacts intra-molecularly with a groove on the surface of the NBD providing a probable means by which conformational changes associated with the nucleotide binding and hydrolysis cycle are conveyed to the transmembrane domain. The MacB NBDs may operate as a conformational switch (16).

MacB confers resistance to antibiotics and supports enterotoxin STII secretion. *E. coli* MacB was first identified and named for its role in macrolide resistance (2), but has since been shown to transport enterotoxin STII (6) and may have a role in protoporphyrin expulsion (17). To identify further MacB substrates, we determined the minimal inhibitory concentrations (MICs) of 11 distinct antimicrobial compounds against *E. coli* strains lacking chromosomal *acrAB* and *macAB* and expressing either plasmid-borne wild type or catalytically-inactive *E. coli* MacAB. The strain used lacks the broad-spectrum RND efflux pump AcrAB facilitating detection of MacAB substrates that might otherwise be obscured. We observed a significant protective effect for MacAB against erythromycin, bacitracin and colistin (**Fig. 2a, SI Appendix, Table S3**). Identification of tolerance to bacitracin and colistin, both of which are cyclic peptides, shows MacB has a broader role in antibiotic resistance than previously recognised and is not limited to macrolides such as erythromycin.

Having shown that MacB handles peptide-like antibiotics such as colistin and bacitracin, we further investigated its role in enterotoxin STII secretion. Enterotoxin STII is a 48-amino acid protein with two internal disulfide bonds that is produced as a virulence factor by enterotoxigenic *E. coli* (**Fig. 2b**). Expression of STII in *E. coli* leads to the appearance of mature toxin in the culture supernatant that is disrupted when chromosomal *macAB* genes are deleted. Secretion of STII is restored by complementation with wild type MacAB, but not by expression of either MacA or MacB alone, or by co-expression of MacAB with an ATPase-inactivating mutation (Glu170Gln) in MacB (**Fig. 2c)**. Our experiments confirm a role for the MacAB-TolC efflux pump in secretion of enterotoxin STII (6, 18) and demonstrate MacB ATPase activity is required to extract this substrate from the periplasm and transport it to the extracellular space (**Fig. 2d**).

Structure-led mutagenesis of *macB* identifies residues involved in antibiotic resistance. To probe the relationship between structure and function in MacB, we used site-directed mutagenesis to disrupt structural features within the NBD, transmembrane domain, stalk and periplasmic domain and tested each variant's ability to confer resistance to erythromycin (**SI Appendix, Table S4**). The MIC results were colour-mapped to a homology model of *E. coli* MacB generated from the

A. actinomycetemcomitans full-length structure and *E. coli* soluble domains (**Fig. 3**). We first targeted residues on the cytoplasmic side of the membrane including residues shown to be mechanistically essential in MacB and other ABC systems (5, 9). As expected, mutation of residues involved in ATP binding (Lys47Ala) and hydrolysis (Glu170Gln) each reduced MIC values to levels comparable with that of the empty vector control (a 32-fold reduction) (**Fig. 3a, d)**. Deletion of the minor coupling helix or disruption of an electrostatic interaction (Arg121-Glu256) between the amphipathic helix and NBD did not significantly affect MacB function showing these features are not essential (**SI Appendix, Table S4**). Next, we focussed on polar residues at the dimer interface. Alanine substitutions for Thr275, Ser285, Ser532, and Asn542 in the MacB transmembrane domain, and residues Thr517 and Thr520 in the periplasmic stalk, did not substantially affect MacB function suggesting these residues are unlikely to interact with substrates. Finally, through extensive mutagenesis of the periplasmic domain, we revealed an obvious 'hotspot' of residues on the interior surface indicating a plausible substrate interaction site (**Fig. 3b, c, d**). Key positions associated with the periplasmic hotspot are Tyr376, Phe444, Trp505 and Thr349, for which alanine substitution yields at least a 16-fold reduction in MIC, and Tyr315, Phe320, Phe503 and Met507 which each give 8-fold reductions. Further MIC determinations for a subset of MacB variants were performed using bacitracin and colistin revealing a similar pattern of MIC reduction to that of erythromycin suggesting the same periplasmic site is important for resistance to all of these molecules (**SI Appendix, Fig. S3** & **Table S5**).

We further tested our 70-strong cohort of MacB variants for their capacity to secrete enterotoxin STII. With the exception of Lys47Ala and Glu170Gln, all MacB variants were capable of toxin secretion (**SI Appendix, Table S4**). The reason for differential effects of periplasmic domain mutations on antibiotic resistance and enterotoxin secretion is not yet clear. One possibility is that the structure of enterotoxin presents multiple opportunities for productive interaction with MacB that render individual point mutations insufficient to disrupt transport. Alternatively, the site of enterotoxin interaction may be distinct from the site identified here relating to antibiotic resistance; a second site could plausibly be located, either in whole, or in part, elsewhere in MacB, or within another component of the tripartite assembly (MacA or TolC). We conclude that individual amino acids lining the interior face of the MacB periplasmic domain are vital for antibiotic resistance but dispensable for enterotoxin secretion, while residues associated with ATP binding and hydrolysis are essential for both.

ATP-bound and nucleotide-free states of MacB reveal the molecular basis of mechanotransmission. We assessed the conformational changes associated with ATP-binding and hydrolysis by comparing our ATP-bound MacB with a nucleotide-free form extracted from a MacAB-TolC assembly structure determined by cryoEM (11) (**Fig. 4**). After superposition of the two MacB

forms, we generated a molecular morph revealing the probable motions that link these states (**Movie 3**). Our comparison reveals distinctive long-range conformational changes in the transmembrane and periplasmic domains linked to the nucleotide status of the NBD that we define here as 'mechanotransmission'. In the nucleotide-free form, the MacB NBDs are separated and a prominent V-shaped split is apparent in the periplasmic stalk (**Fig. 4a** *left*). The periplasmic head of MacB adopts an 'open' form with an obvious cavity between the two monomers (**Fig. 4b**). In the ATP-bound state, the cytoplasmic domains are dimerized and the two halves of the periplasmic stalk stand straight and perpendicular to the plane of the membrane (**Fig. 4a** *right*). In this form, the cavity within the periplasmic domain is absent and the entire structure is much more compact (**Fig. 4c**). Conformational changes apparent on both sides of the membrane are coordinated by the transmembrane domain, stalk and coupling helices. Specifically, upon ATP binding, NBD dimerization acts through the major coupling helix to push TM2 upwards through the membrane causing a shift in the register of opposing residues on either side of the dimer interface. The newly generated interface promotes association of the transmembrane domain and stalk into a rigid 4-helix bundle bringing together the periplasmic domains. Details of the dimer interface observed for each conformation are given in **SI Appendix, Fig. S4**.

To validate the conformational changes observed by comparison of MacB structures, we used a disulfide cross-linking experiment testing whether restricting mechanotransmission impacts on activity. Guided by the structure, we produced a MacB cysteine variant (Thr517Cys) predicted to lock the stalk in its closed ('zipped') conformation and tested its ability to confer erythromycin tolerance (**SI Appendix, Fig. S5a-c & Table S6**). Consistent with inhibition of MacB due to disulfide locking, the Thr517Cys variant has a lower than wild type MIC that is further diminished by addition of $CuCl_2$ (an oxidant favouring disulfide formation) and restored to wild type levels by DTT (favouring disulfide reduction). Contrastingly, the activities of the wild type, Glu170Gln and Thr517Ala variants are unaffected by either $CuCl_2$ or DTT. The cysteine cross-linking experiment provides *in vivo* support for the mechanotransmission mechanism.

A molecular bellows mechanism for the MacAB-TolC tripartite efflux pump. We considered how MacB mechanotransmission might operate within the context of the assembled MacAB-TolC pump to drive substrate from the periplasm to the extracellular space. The structure of the nucleotide-free MacAB-TolC complex is known (11) and superposition of our ATP-bound MacB structure suggests a model for the missing assembled state. The model suggests the MacA hexamer accommodates MacB in both of its two conformational states and that a tight seal between these components is maintained throughout the mechanotransmission cycle. An interior cavity at the interface between MacA and MacB undergoes dramatic changes in volume upon transition between nucleotide-free and ATP-bound

forms (**SI Appendix, Fig. S6)** leading us to suggest that the assembled MacAB-TolC complex acts as a 'molecular bellows' during efflux (**SI Appendix, Fig. 5a, b**).

In the molecular bellows mechanism (**SI Appendix, Fig. 5a, b**), substrates are proposed to enter the interior cavity via an opening in MacB located between parted periplasmic domains and stalk (see also **Fig. 4a,** *left*) before subsequent ATP-binding causes closure of the periplasmic domain by mechanotransmission. The reduction in interior cavity volume forces the contents of the MacB periplasmic domain, under pressure, through the MacA gate ring, previously suggested to act as a one-way valve (11). Once the pressure on either side of the gate has equalised, the gate ring relaxes to its closed resting state preventing backflow of substrates. ATP hydrolysis then resets the system with further substrates and solvent necessary to refill the cavity entering from the periplasm as the interior cavity expands.

Coordination of the ATP-binding and hydrolysis cycle with detection of the substrate in the periplasmic cavity is likely to be regulated to prevent wasteful expenditure of ATP. Whether MacB has a role in sensing the 'readiness' of periplasmic-bound substrates for export is unclear, but it is known that the MacA N-terminus spans the inner membrane and stimulates MacB ATPase activity suggesting the adaptor plays a role in mediating this signal (5, 19).

MacB represents a superfamily of mechanotransmissive ABC transporters including LolCDE and FtsEX. We next examined the degree to which structural features underpinning the mechanotransmission mechanism in MacB are conserved in related proteins. MacB belongs to a large and functionally-diverse monophyletic group of ABC transporters (sometimes termed the ABC3 superfamily) that has been defined based on sequence-level features including hydropathy profiles and amino acid similarity (12, 13). Many homologues of MacB are genetically encoded in operons alongside genes for a periplasmic adaptor and TolC-like protein suggesting they form TEPs similar to MacAB-TolC. Two examples are PvdT of *Pseudomonas aeruginosa* (20) and AatP from enteroaggregative *E. coli* (21). Like MacAB-TolC, these TEPs extract their substrates from the periplasm and use cytoplasmic ATP hydrolysis to power efflux across the outer membrane. Other homologues of MacB do not form TEPs, but do couple cytoplasmic ATP hydrolysis with activities in the periplasm or extracytoplasmic space. LolC and LolE collaborate with NBDs encoded by LolD to translocate lipoproteins from the outer face of the inner membrane to a periplasmic chaperone during outer membrane biogenesis (14). Similarly, FtsE (NBD) and FtsX (transmembrane domain) form a substrateless ABC transporter involved in transmembrane signalling between cytoplasmic and periplasmic components of the cell division machinery (15, 22). Hydropathy plots show that PvdT, AatP, LolC, LolE and FtsX all have the same transmembrane topology as MacB, with a periplasmic domain located between the first and second membrane spanning helices (**Fig. 6a**). Secondary

structure analysis predicts that all these proteins except FtsX contain both the Porter and Sabre subdomains present in the MacB crystal structure (**Fig. 6b**). For FtsX, the presence of the Porter and absence of the Sabre is confirmed by its crystal structure from *M. tuberculosis*. However, our prediction for LolCDE conflicts with previous suggestions that the periplasmic domain may have a β-barrel fold similar to LolA and LolB (23). Assigning the correct fold to LolC is essential because the previously proposed 'mouth-to-mouth' transfer of lipoprotein substrates from LolCDE to LolA is not compatible with a MacB-like fold. We experimentally tested our prediction by solving the crystal structure of the *E. coli* LolC periplasmic domain. Data collection and refinement statistics are provided in **SI Appendix, Table S7** and the LolC periplasmic domain is shown in comparison with those of MacB and FtsX in **Fig. 6c.** The 1.88 Å structure of LolC confirms a MacB-like fold with both Sabre **(Fig. 6d**) and Porter (**Fig. 6e**) subdomains (**Movie 4**). We conclude that features of the MacB architecture underpinning its distinctive mechanotransmission mechanism, including transmembrane topology and core aspects of its extracytoplasmic domain structure, are conserved throughout this ABC superfamily.

DISCUSSION

We determined the crystal structure of MacB in an ATP-bound conformation revealing a new ABC transporter fold (**Fig. 1**) and discovered that MacB confers resistance to cyclic peptides such as bacitracin and colistin in addition to expelling the known substrates erythromycin and enterotoxin STII (**Fig. 2**). Structure-guided mutagenesis of MacB led to identification of residues in the periplasmic domain essential for erythromycin tolerance (**Fig. 3**) and comparison of ATP-bound and nucleotide-free structures of MacB revealed allosteric coupling of periplasmic conformational change with reversible dimerization of the cytoplasmic NBDs (**Fig. 4**). We term the distinctive transmembrane conformational coupling mechanism of MacB 'mechanotransmission' and propose that it is harnessed within the context of the assembled tripartite efflux pump to drive substrate efflux from the periplasm to the extracellular space by acting as a 'molecular bellows' (**Fig. 5**). Finally, we demonstrate that the structural architecture underlying mechanotransmission is present in homologous systems such as the LolCDE lipoprotein trafficking complex and FtsEX cell division machinery (**Fig. 6**) suggesting a unified mechanism for the entire superfamily.

The key feature of MacB that distinguishes it from other ABC transporters is its mechanotransmission mechanism (**Fig. 4, Movie 3**). Neither ATP-bound nor nucleotide-free structures of MacB reveal evidence of a central pore through which substrates might be passed, nor does either exhibit the characteristic inward- and outward-facing cavities that are the hallmark of alternating-access mechanism. MacB operates solely through extracytoplasmic conformational change driven by cytoplasmic ATP hydrolysis. In collaboration with the MacA adaptor and TolC exit duct, MacB powers the expulsion of enterotoxin STII from periplasm to extracellular space and it seems likely that

antibiotic substrates of MacB (erythromycin, colistin and bacitracin) take the same route, rather than being driven across the inner membrane as previously thought. Alternatively, it is possible that MacB does not interact directly with antibiotics, but instead transports another, as-yet-unidentified factor affecting the cell's susceptibility. Outer membrane glycolipids have been implicated as potential substrates for MacAB-TolC (24), and such substrates could conceivably drive resistance indirectly by modifying permeability of the cell envelope.

MacB's role in erythromycin resistance partially overlaps that of the RND family tripartite efflux pump AcrAB-TolC. RND family TEPs, including AcrAB-TolC, have been described as 'periplasmic vacuum cleaners' (25) on account of their broad substrate specificity. While AcrAB-TolC is highly proficient in secretion of small molecules, including erythromycin, enterotoxin STII is solely exported via MacAB-TolC. Systems homologous to MacAB-TolC secrete pyoverdine (a peptide-like siderophore from *P. aeruginosa* (20)) and dispersin (a 10 kDa enteroaggregative *E. coli* signalling protein (21)) which suggests a division of labour where RND transporters tackle small molecule efflux and MacAB-TolC-based systems drive export of larger peptides and small proteins.

The structural architecture of MacB is conserved in both FtsEX and LolCDE (**Fig. 6**) suggesting the capacity for mechanotransmission is also preserved. FtsEX regulates periplasmic peptidoglycan hydrolases during cell division (15, 22, 26) while LolCDE extracts lipoproteins from the outer-leaflet of the bacterial inner membrane and presents them to the periplasmic chaperone LolA for trafficking to the outer membrane (14, 27). Roles for mechanotransmission in these processes remain to be fully elucidated, however, for LolCDE, the upward force generated by zipping together of the periplasmic stalk could aid lipoprotein extraction from the bacterial membrane. Similarly, for FtsEX, the two conformational states could form a molecular switch, stimulating recruitment and/or activation of extracytoplasmic enzymes in one conformation and frustrating this process in the other. The MacB structures constitute a valuable tool for guiding future research on FtsEX and LolCDE both of which are key antibiotic targets (28, 29).

Intriguingly, the LptBFG complex has a similar function to LolCDE but an entirely different transmembrane topology (30). The use of several distinct structural folds to direct similar *in vivo* functions is a recurring feature of ABC transporter evolution as evidenced by the three different ABC superfamilies linked to substrate import (**SI Appendix, Fig. S1** - Types I, II and III) and further two associated with substrate export (**SI Appendix, Fig. S1** - Types IV and V). It will be interesting to compare the mechanism of MacB/LolCDE (Type VII) with that of LptBFG (Type VI) once further conformational states of the latter are known.

In summary, the MacB structure defines a new ABC transporter superfamily and reveals the mechanotransmission mechanism it uses. MacB superfamily members do not transport substrates across the inner membrane in which they reside, but instead, couple cytoplasmic ATP hydrolysis to extracytoplasmic conformational change. Whether mechanotransmission is used to gate access to an outer membrane exit duct (as for MacB), pass a substrate from the membrane to a chaperone (LolCDE), or else regulate the activity of periplasmic enzymes (FtsEX), the same underlying 4-transmembrane helix architecture provides the means of transmitting conformational change across the membrane. The MacB architecture provides a fresh structural and mechanistic perspective on a plethora of homologous 'mechanotransmissive ABC transporters' that mediate diverse biological functions in the bacterial envelope and extracellular space.

METHODS

Detailed **Supplementary Methods** are available online. Briefly, *Aggregatibacter actinomycetemcomitans* MacB was expressed with an N-terminal His-tag in *E. coli* C43 (DE3) before purification in lauryl maltose neopentyl glycol as a stabilising detergent. MacB was crystallised in two distinct crystal forms in the presence of either ATPγS or ATP and the structures solved by a combination of molecular replacement and selenomethionine phasing methods. Structures of the *E. coli* MacB periplasmic domain (residues 309-508) and cytoplasmic NBD (residues 1-223) were determined to aid this phasing strategy. Minimum inhibitory concentrations were assessed by serial dilution method in *E. coli* C43Δ*acrAB*Δ*macAB* with either wild type or variant MacB co-expressed with MacA from a plasmid. Enterotoxin STII secretion was assessed by trichloroacetic acid precipitation of culture supernatants and analysed by SDS-PAGE. Molecular morphs used a homology model of *E. coli* MacB based on the *A. actinomycetemcomitans* ATP-bound state and the nucleotide-free state extracted from 5NIL (11) as start and end points. Bioinformatic analysis used TMPred for hydropathy plots and Promals3D (31) for secondary structure prediction and sequence alignment. The *E. coli* LolC periplasmic domain (residues 48-266) was expressed with a C-terminal His-tag in *E. coli* BL21 (DE3) and the structure solved by molecular replacement using the *Aa*MacB periplasmic domain. All structures were deposited in protein databank: accession codes 5LIL, 5LJ6, 5LJ7, 5LJ8, 5LJ9, 5LJA and 5NAA.

ACKNOWLEDGEMENTS

We thank staff at Soleil (France) and Diamond (UK) synchrotrons for beam line facilities and Professor Yamanaka for providing the pET11-STII plasmid. This work was supported by grants from the UK Medical Research Council and the Wellcome Trust.

REFERENCES

1. Hinchliffe P, Symmons MF, Hughes C, Koronakis V (2013) Structure and operation of bacterial tripartite pumps. *Annu Rev Microbiol* 67:221–42.
2. Kobayashi N, Nishino K, Yamaguchi A (2001) Novel macrolide-specific ABC-type efflux transporter in

Escherichia coli. *J Bacteriol* 183(19):5639–5644.

3. Koronakis V, Sharff A, Koronakis E, Luisi B, Hughes C (2000) Crystal structure of the bacterial membrane protein TolC central to multidrug efflux and protein export. *Nature* 405(6789):914–9.
4. Lu S, Zgurskaya HI (2012) Role of ATP binding and hydrolysis in assembly of MacAB-TolC macrolide transporter. *Mol Microbiol* 86(5):1132–1143.
5. Tikhonova EB, Devroy VK, Lau SY, Zgurskaya HI (2007) Reconstitution of the *Escherichia coli* macrolide transporter: The periplasmic membrane fusion protein MacA stimulates the ATPase activity of MacB. *Mol Microbiol* 63(3):895–910.
6. Yamanaka H, Kobayashi H, Takahashi E, Okamoto K (2008) MacAB is involved in the secretion of *Escherichia coli* heat-stable enterotoxin II. *J Bacteriol* 190(23):7693–7698.
7. Dreyfus LA, et al. (1993) Calcium influx mediated by the *Escherichia coli* heat-stable enterotoxin B (STB). *Proc Natl Acad Sci U S A* 90(8):3202–3206.
8. Locher KP (2016) Mechanistic diversity in ATP-binding cassette (ABC) transporters. *Nat Struct Mol Biol* 23(6):487–93.
9. ter Beek J, Guskov A, Slotboom DJ (2014) Structural diversity of ABC transporters. *J Gen Physiol* 143(4):419–435.
10. Kobayashi N, Nishino K, Hirata T, Yamaguchi A (2003) Membrane topology of ABC-type macrolide antibiotic exporter MacB in *Escherichia coli*. *FEBS Lett* 546(2–3):241–246.
11. Fitzpatrick AWP, et al. (2017) Structure of the MacAB–TolC ABC-type tripartite multidrug efflux pump. *Nat Microbiol* 2(May):17070.
12. Khwaja M, Ma Q, Saier MH (2005) Topological analysis of integral membrane constituents of prokaryotic ABC efflux systems. *Res Microbiol* 156(2):270–277.
13. Wang B, Dukarevich M, Sun EI, Yen MR, Saier MH (2009) Membrane porters of ATP-binding cassette transport systems are polyphyletic. *J Membr Biol* 231(1):1–10.
14. Yakushi T, Masuda K, Narita S, Matsuyama S, Tokuda H (2000) A new ABC transporter mediating the detachment of lipid-modified proteins from membranes. *Nat Cell Biol* 2(4):212–218.
15. Yang DC, et al. (2011) An ATP-binding cassette transporter-like complex governs cell-wall hydrolysis at the bacterial cytokinetic ring. *Proc Natl Acad Sci* 108(45):E1052–E1060.
16. Higgins CF, Linton KJ (2004) The ATP switch model for ABC transporters. *Nat Struct Mol Biol* 11(10):918–926.
17. Turlin E, et al. (2014) Protoporphyrin (PPIX) efflux by the MacAB-TolC pump in *Escherichia coli*. *Microbiologyopen* 3(6):849–859.
18. Foreman DT, Martinez Y, Coombs G, Torres A, Kupersztoch YM (1995) TolC and DsbA are needed for the secretion of STB, a heat-stable enterotoxin of *Escherichia coli*. *Mol Microbiol* 18(2):237–245.
19. Modali SD, Zgurskaya HI (2011) The periplasmic membrane proximal domain of MacA acts as a switch in stimulation of ATP hydrolysis by MacB transporter. *Mol Microbiol* 81(4):937–951.
20. Imperi F, Tiburzi F, Visca P (2009) Molecular basis of pyoverdine siderophore recycling in *Pseudomonas aeruginosa*. *Proc Natl Acad Sci U S A* 106(48):20440–20445.
21. Nishi J, et al. (2003) The Export of Coat Protein from Enteroaggregative *Escherichia coli* by a Specific ATP-binding Cassette Transporter System. *J Biol Chem* 278(46):45680–45689.

22. Du S, Pichoff S, Lutkenhaus J (2016) FtsEX acts on FtsA to regulate divisome assembly and activity. *Proc Natl Acad Sci U S A* 113(34):E5052-61.
23. Okuda S, Tokuda H (2009) Model of mouth-to-mouth transfer of bacterial lipoproteins through inner membrane LolC, periplasmic LolA, and outer membrane LolB. *Proc Natl Acad Sci U S A* 106(14):5877–82.
24. Lu S, Zgurskaya HI (2013) MacA, a periplasmic membrane fusion protein of the macrolide transporter MacAB-TolC, binds lipopolysaccharide core specifically and with high affinity. *J Bacteriol* 195(21):4865–4872.
25. Aires JR, Nikaido H (2005) Aminoglycosides are captured from both periplasm and cytoplasm by the AcrD multidrug efflux transporter of *Escherichia coli*. *J Bacteriol* 187(6):1923–9.
26. Mavrici D, et al. (2014) *Mycobacterium tuberculosis* FtsX extracellular domain activates the peptidoglycan hydrolase, RipC. *Proc Natl Acad Sci U S A* 111(22):8037–42.
27. Narita S, Tokuda H (2016) Bacterial lipoproteins; biogenesis, sorting and quality control. *Biochim Biophys Acta - Mol Cell Biol Lipids*.
28. McLeod SM, et al. (2015) Small-molecule inhibitors of gram-negative lipoprotein trafficking discovered by phenotypic screening. *J Bacteriol* 197(6):1075–82.
29. Lock RL, Harry EJ (2008) Cell-division inhibitors: new insights for future antibiotics. *Nat Rev Drug Discov* 7(4):324–338.
30. Luo Q, et al. (2017) Structural basis for lipopolysaccharide extraction by ABC transporter $LptB_2FG$. *Nat Struct Mol Biol* 24(5):469–474.
31. Pei J, Kim B-H, Grishin N V. (2008) PROMALS3D: a tool for multiple protein sequence and structure alignments. *Nucleic Acids Res* 36(7):2295–2300.
32. Sukumar M, et al. (1995) The structure of *Escherichia coli* heat-stable enterotoxin b by nuclear magnetic resonance and circular dichroism. *Protein Sci* 4(9):1718–1729.

FIGURES

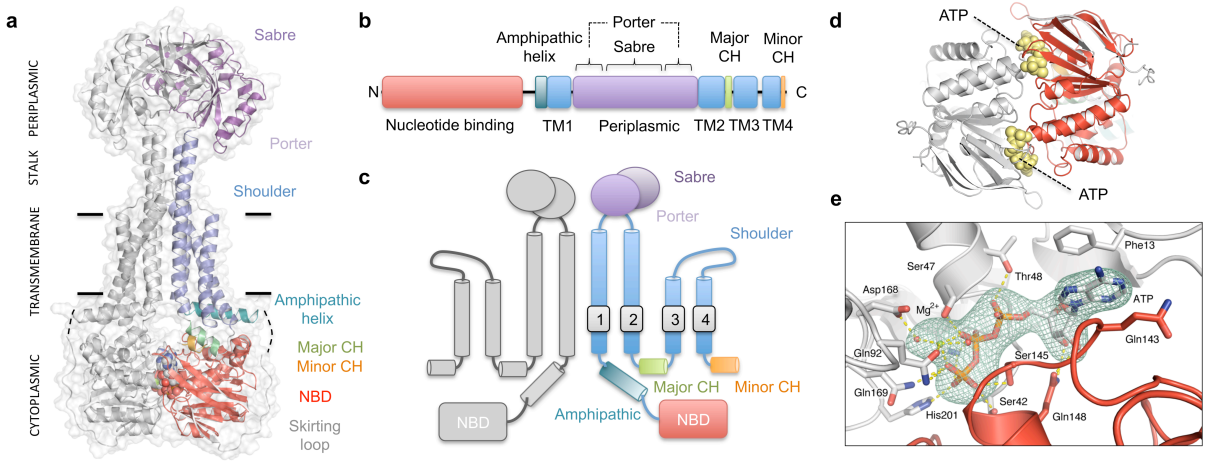

Figure 1: Crystal structure of *A. actinomycetemcomitans* MacB with bound ATP. (a) Overall structure of the MacB dimer. (b) Linear domain organisation of the MacB polypeptide. (c) Topology of MacB. (d) Location of the two ATP molecules (*yellow*) clamped between the nucleotide binding domains (NBDs). (e) Detailed view of bound ATP with omit map density contoured at 3.5 sigma (*teal*). Residues interacting with ATP are labelled and potential hydrogen bonds (*dashed yellow lines*) are indicated. Colouring is consistent across the figure, one monomer is shown in grey and the second is coloured according to the domain arrangement.

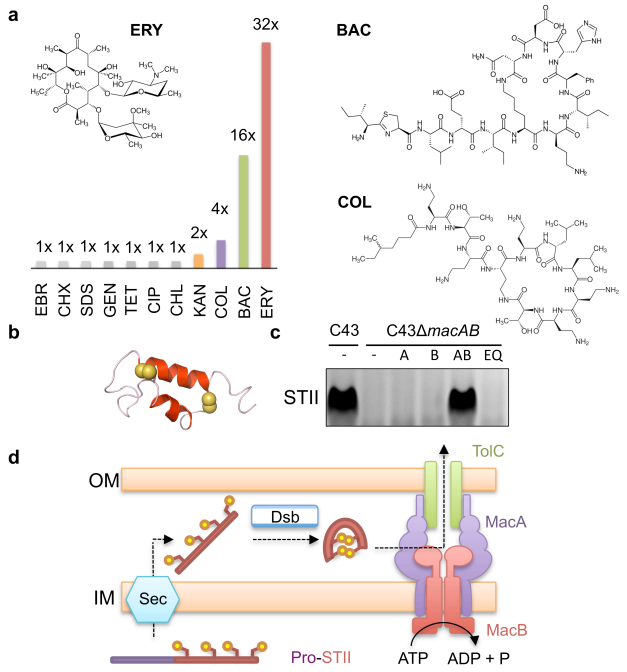

Figure 2: Functional analysis of *E. coli* MacAB-TolC *in vivo*. (a) Antibiotic susceptibility comparison between *E. coli* C43 (DE3) Δ*acrAB*Δ*macAB* cells expressing *E. coli* MacA and either wild type or Glu170Gln *E. coli* MacB variant. The ratio of the MIC for the wild type MacB to the Glu170Gln variant is shown graphically for ethidium bromide (EBR), chlorhexidine (CHX), SDS, gentamycin (GEN), tetracycline (TET), ciprofloxacin (CIP), chloramphenicol (CHL), kanamycin (KAN), colistin (COL), bacitracin (BAC) and erythromycin (ERY). Structures of erythromycin, bacitracin and colistin are shown inset. (b) Structure of enterotoxin STII with disulfide bond-forming sulfur atoms (*yellow spheres*) (PDB: 1EHS) (32). (c) Detection of secreted enterotoxin in *E. coli* culture supernatants by SDS-PAGE. Lanes from left to right, C43 wild type, C43*ΔmacAB*, C43*ΔmacAB* expressing plasmid-borne *macA* (A), *macB* (B), *macAB* (AB), or *macAB* with an ATPase inactivating Glu170Gln substitution (EQ). All strains contain a plasmid expressing enterotoxin STII. (d) Model for two-step secretion of enterotoxin STII across the *E. coli* cell envelope. Sec and Dsb represent the general protein secretion machinery and disulfide bond incorporation systems, respectively.

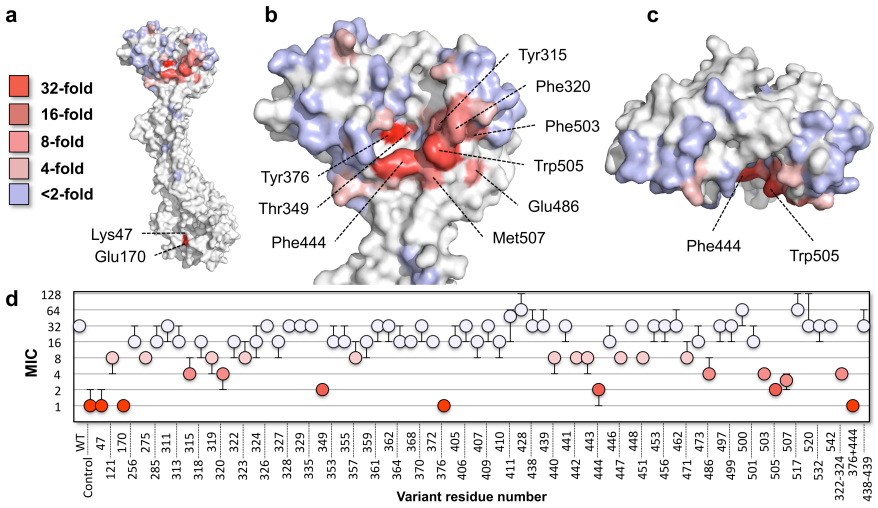

Figure 3: Structure-based mutational analysis of *E. coli* MacB. Erythromycin resistance of C43 (DE3) Δ*acrAB* Δ*macAB* cells expressing *E. coli* MacA and variant MacB mapped to a model of one monomer of *E. coli* MacB. Key indicates the fold decrease in MIC relative to cells expressing wild type MacAB. (a) The MacB monomer presenting the dimer interface. (b) Close-up view of the periplasmic domain. (c) Top-down view of the MacB periplasmic domain. (d) Minimum inhibitory concentrations (MICs, μg/ml) for the 70 MacB variants tested. Homology model shown is based on our full-length *A. actinomycetemcomitans* MacB crystal structure and high-resolution structure of the *E. coli* MacB periplasmic domain.

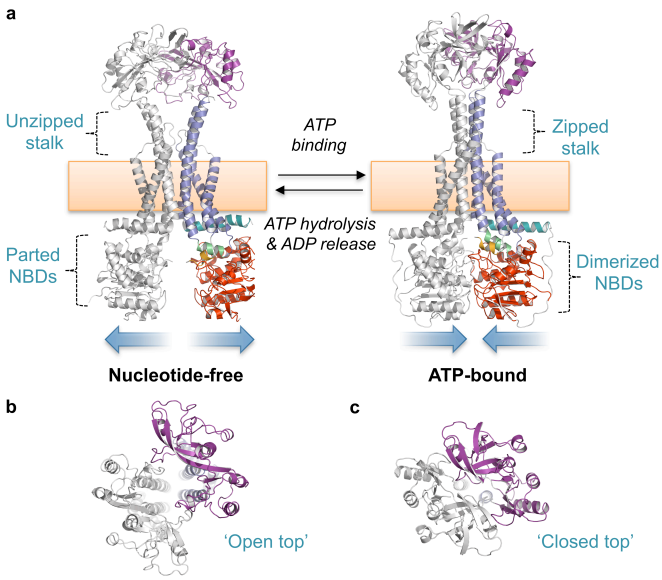

Figure 4: Mechanotransmission mechanism of MacB. (a) Nucleotide-free (*left*) and ATP-bound MacB (*right*). (b) Top-down view of the MacB dimer showing the open head of the nucleotide-free form. (c) Equivalent view of the ATP-bound form showing closure of the periplasmic dimer. Domains of MacB coloured as in **Figure 1.** Both models represent *E. coli* MacB, the nucleotide-free form is extracted from the cryoEM structure of the MacAB-TolC complex (5NIL) and the ATP-bound form is a homology model generated from our crystal structure of the nucleotide-bound *A. actinomycetemcomitans* MacB (5LIL). A full molecular morph between the two states is presented in **Movie 3**.

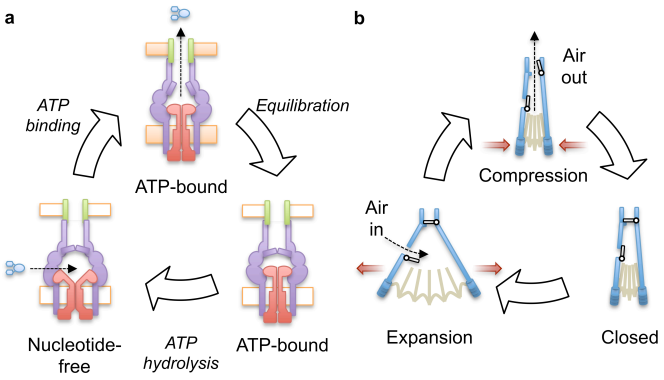

Figure 5: A 'molecular bellows' mechanism for substrate secretion by the MacAB-TolC tripartite efflux pump. (a) Proposed catalytic cycle of the MacAB-TolC efflux pump. MacB (*red*), MacA (*purple*), TolC (*green*) and substrate (*blue*). (b) Operation of a fireplace bellows.

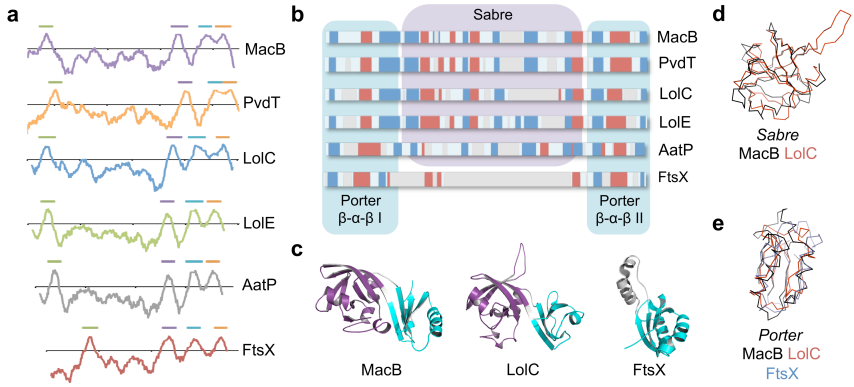

Figure 6: MacB is the archetypal member of a topological unique ABC superfamily. (a) Hydropathy profile of MacB and five key homologues demonstrating a common 4-transmembrane helix topology. Horizontal bars above the plots indicate TM helices. (b) Comparison of secondary structure predictions for the periplasmic domain located between TM1 and TM2 for MacB and homologues. Beta sheets (*blue*), alpha helices (*red*) and alignment gaps (*grey*) are shown. (c) Periplasmic domain structures of MacB, LolC and FtsX. Sabre subdomain shown in *purple*, Porter subdomain *cyan*. (d) Superposition of Sabre subdomains from MacB and LolC. (e) Superposition of Porter subdomains from MacB, LolC and FtsX.

Supporting Information Appendix

Structure and mechanotransmission mechanism of the MacB ABC transporter superfamily

Allister Crow, Nicholas P. Greene*, Elise Kaplan, Vassilis Koronakis*

**Joint first authorship*

Supplemental Figures

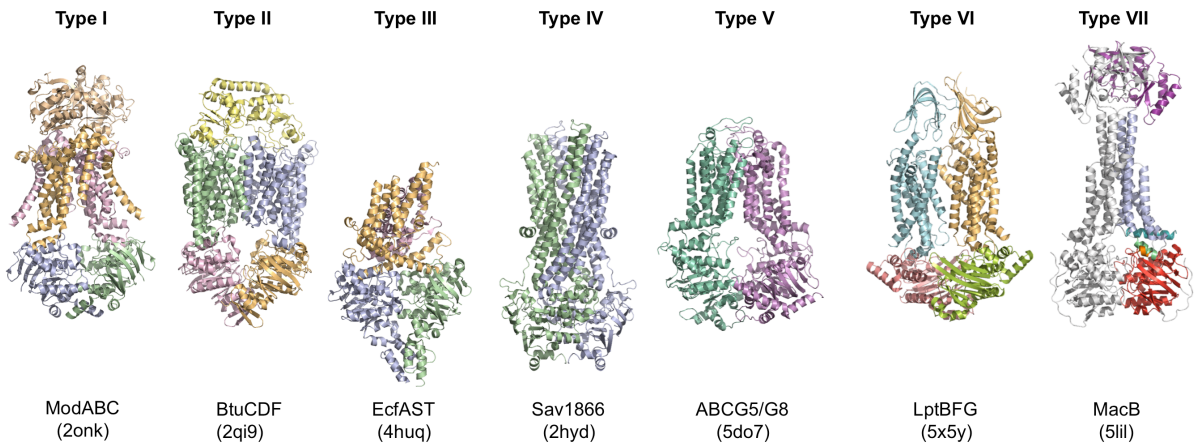

Figure S1: Seven ABC transporter superfamilies. ABC transporters of known structure fall into seven distinct superfamilies that are readily discerned by their 3-dimensional fold. An example from each superfamily is presented. From left to right the molybdate transporter (1) (ModABC), vitamin B_{12} transporter (2) (BtuCDF), folate importer (3) (EcfAST), multidrug exporter (4) (Sav1866), the sterol transporter (5) (ABCG5/G8), LPS extractor (6) (LptBFG) and the enterotoxin and macrolide transporter (MacB). Folds are named by extension of a previously established convention (7). PDB codes are shown in parentheses.

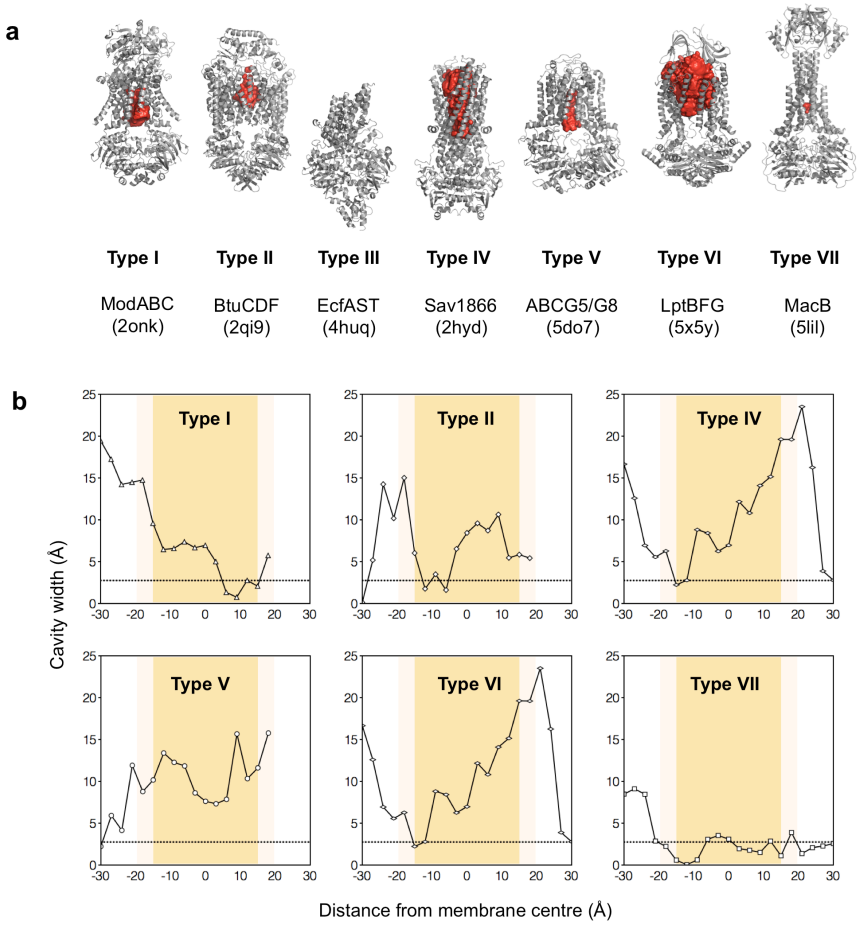

Figure S2: Intramembrane cavity analysis for ABC transporter superfamilies. (a) Visualisation of central transmembrane cavities as solid red 'casts' produced using HOLLOW (8). Sav1866 (4) and BtuCDF (2) are in outward-facing conformations, ModABC (1) and ABCG5/G8 (5) are both inward facing. MacB does not possess any significant cavities in either the transmembrane domain or periplasmic stalk. (b) Plots of cavity diameter at 3 Å intervals across the membrane region, from cytoplasm (-30 Å) to periplasm (+30 Å), are shown for MacB and five other ABC transporters. The 30 Å hydrophobic membrane core is shaded orange (-15 Å to +15 Å) with the lipid head group region in a lighter tone. The horizontal line represents the diameter of a water molecule (2.75 Å), only the region above the horizontal dotted line is solvent accessible. Analysis used the PoreWalker server (9).

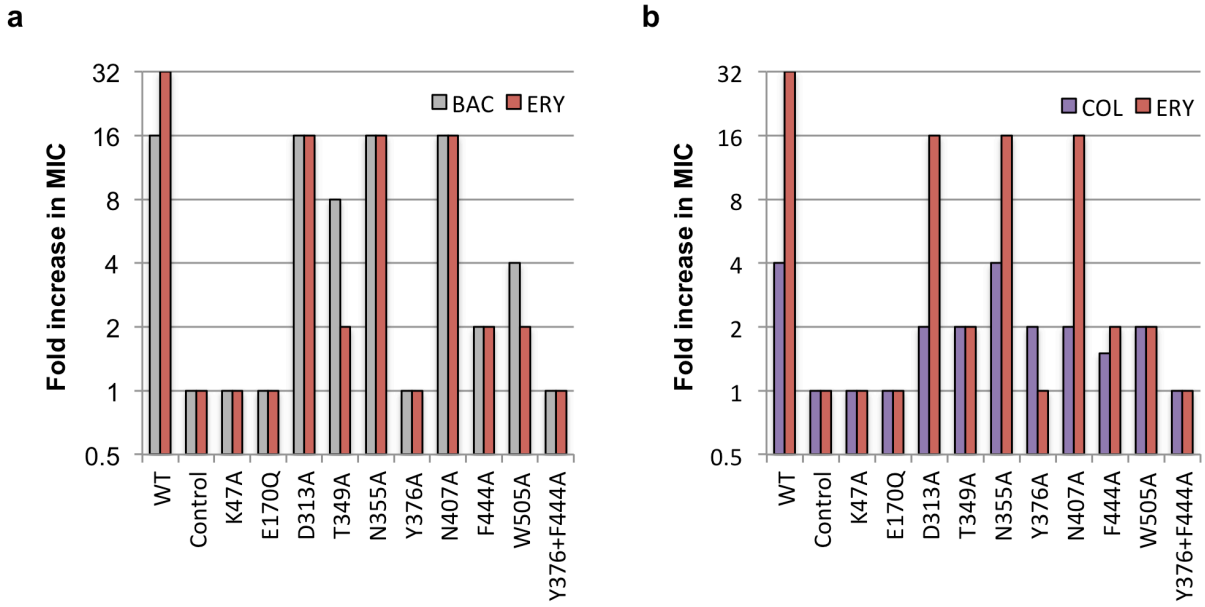

Figure S3: MacB periplasmic domain variants impaired in erythromycin tolerance have similar impairments in bacitracin and colistin resistance. (a) Comparison of bacitracin MIC data with erythromycin. (b) Comparison of colistin MIC data with erythromycin. Coloured bars represent fold increase in median MIC using the E170Q variant as the reference. Full details of the MIC data are provided in **Table S5**.

Figure S4

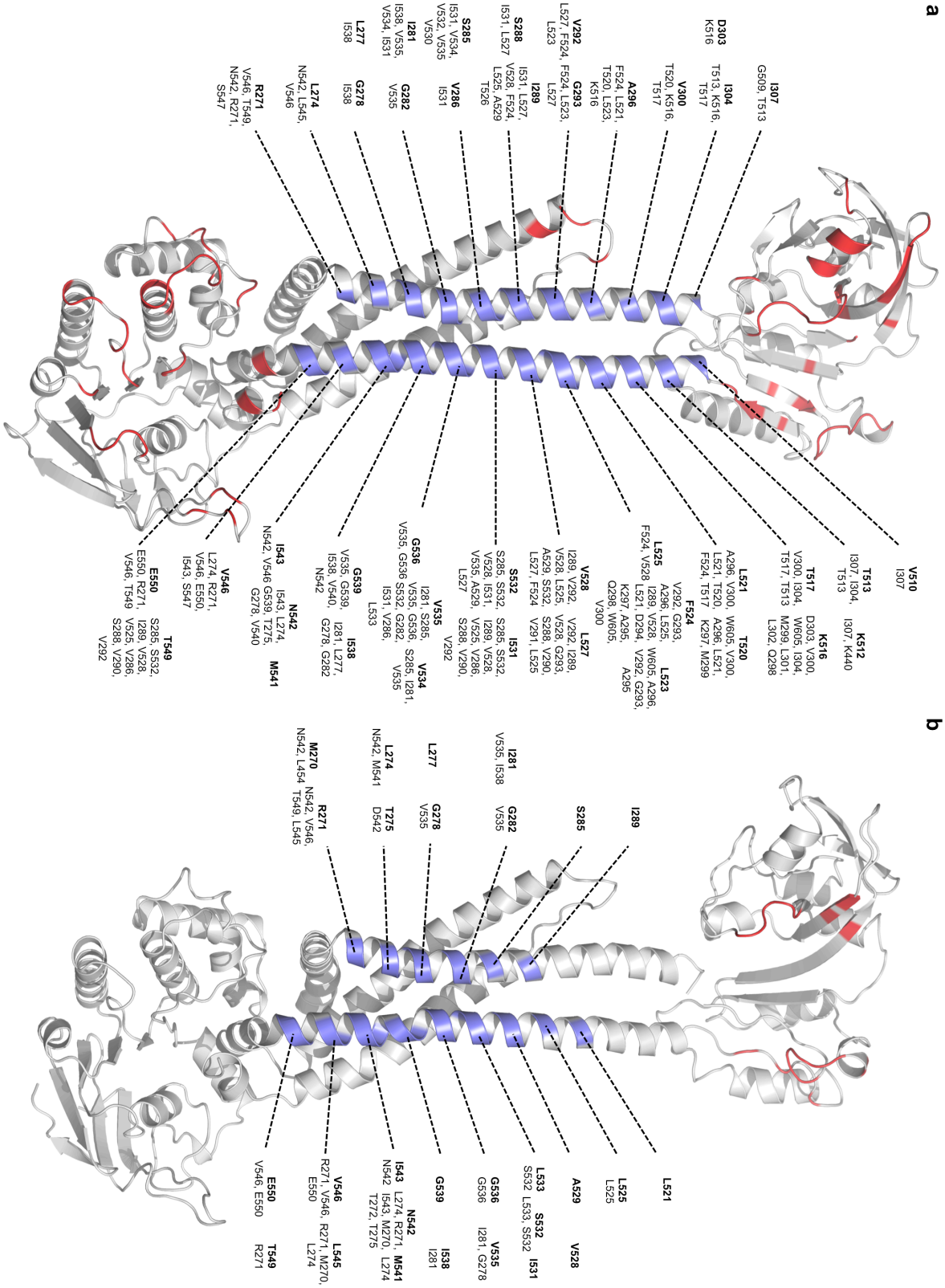
a
V510
I307
T513
I307, I304,
T513
K512
I307, K440
K516
D303, V300,
W605, I304,
M299, L301,
L302, Q298
T517
V300, I304,
T517, T513
L521
A296, V300,
L521, T520,
F524, T517
T520
A296, V300,
L521, T520,
A296, L521,
K297, M299
F524
V292, Q293,
A296, L525,
I289, V528,
K297, A295,
Q298, W605,
V300
L523
W605, A296,
V292, Q293,
A295
L525
F524, V528
V528
I289, V292,
V528, L525,
A529, S532,
L527, F524
L527
V292, I289,
V528, Q293,
S288, V290,
V291, L525
S531
S285, S532,
V528, I531,
V535, A529,
L527
S532
S285, S532,
I289, V528,
V525, V286,
S288, V290,
V292
V534
I281, S285,
V535, G536,
S285, I281,
V535
V535
V535, G536
S532, G282,
I531, V286,
L533
I538
I281, L277,
G278, G282
G539
V535, G539,
I538, V540,
N542
N542
I543, L274,
G539, T275,
G278, V540
M541
I543
N542, V546
V546
L274, R271,
V546, E550,
I543, S547
E550
S285, S532,
I289, V528,
V525, V286,
S288, V290,
V292
T549
V546, T549,
N542, R271,
S547
R271
L274, L545,
V546
L274
I538
G278
V535
G282
I531
S288
L527,
L523
V292
I538,
V534,
I281
V530
S285
V532,
V534,
I531
V286
I307
G509, T513
I304
T513, K516,
T517
D303
K516
V300
T520, K516,
T517
A296
F524, L521,
T520, L523,
K516
G293
L527, F524,
L523
I289
I531, L527,
V528, F524,
L525, A529,
T526
b
I289
S285
G282
V535
I281
V535, I538
L277
G278
V535
L274
N542, M541
T275
D542
R271
N542, V546,
T549, L545
M270
N542, L454
L521
L525
A529
V528
L533
S532
S532
L533, S532
I531
G536
G536
I281, G278
V535
I538
I281
G539
N542
I543
N542
L274, R271,
I543, M270,
T272, T275
M541
L274
V546
R271, V546,
E550
L545
R271, M270,
L274
E550
V546, E550
T549
R271

Figure S4: Dimer interfaces for ATP-bound and nucleotide-free MacB. (a) Face-on view of the interface for a monomer of an *E. coli* MacB homology model based on the ATP-bound *A. actinomycetemcomitans* MacB structure. (b) Equivalent view of a monomer from *E. coli* MacB extracted from the cryoEM structure of the MacAB-TolC assembly (5NIL). Residues at the interface were identified with PISA (10) and contact sites defined using a 5 Å cut-off. Contact residues belonging to either TM1 or TM2 are coloured blue, and contacts elsewhere are coloured red. Residues belonging to TM1 or TM2 are annotated in bold with residues they contact across the dimer interface noted beneath in plain font. For clarity, residues falling on the same 'rung' of a helix are noted side-by-side with a single marker drawn to locate that rung on the structure.

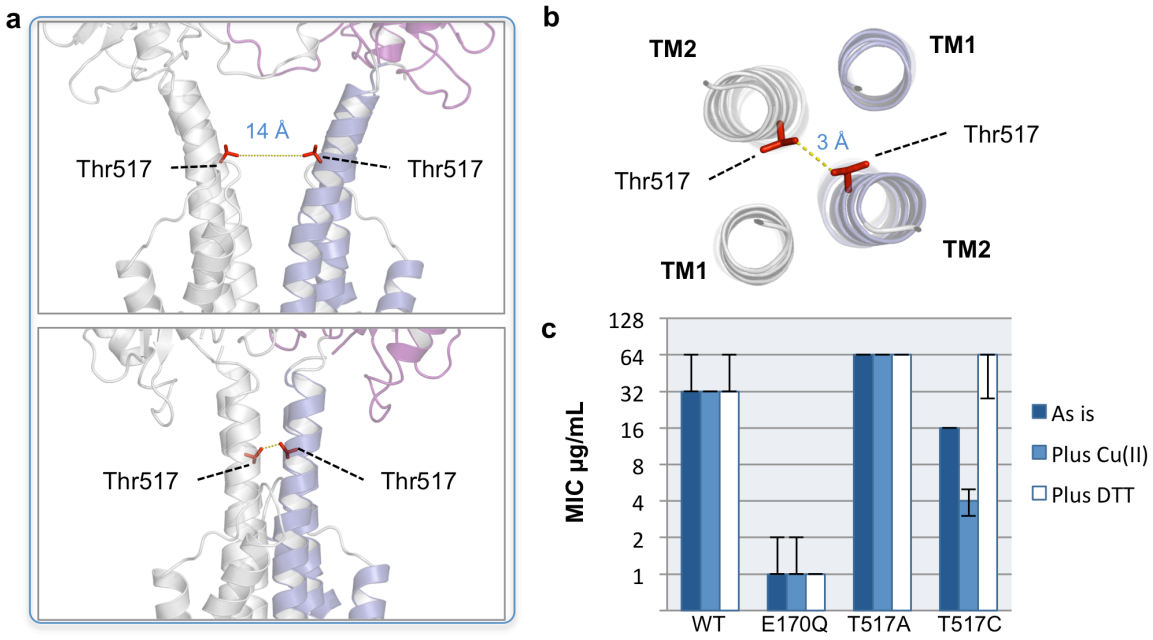

Figure S5: Locking the MacB periplasmic stalk using cysteine disulfide cross-links. (a) Location of Thr517 in nucleotide-free (*top*) and ATP-bound MacB (*bottom*). (b) Top-down view of the stalk showing position of Thr517 in the dimer interface. (c) MacB activity assessed using erythromycin MIC data. Coloured bars represent median values with the interquartile range shown as a black line.

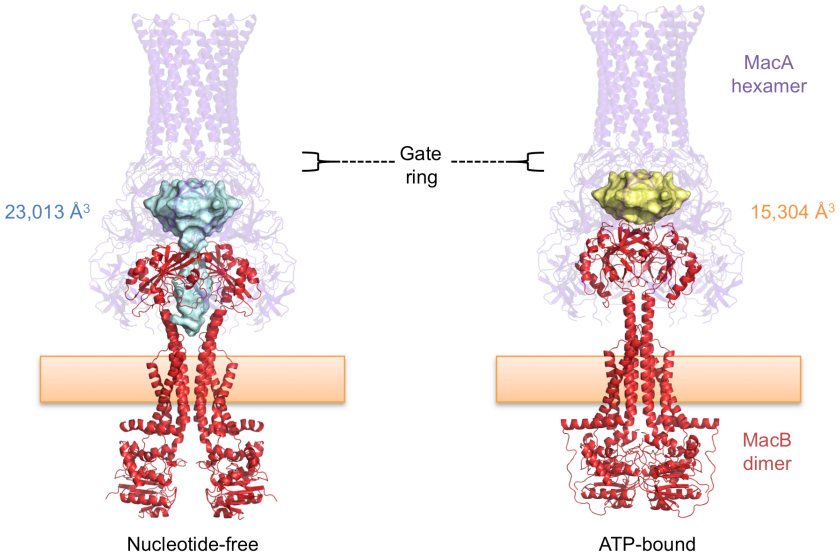

Figure S6: Volumetric analysis of the MacAB-TolC assembly. A central cavity at the interface between MacA and MacB undergoes a significant decrease in volume upon closure of the MacB periplasmic domains during ATP-binding. Models of the assembly in nucleotide-free and ATP-bound forms are shown on the *left* and *right*, respectively. Cavities are shown as solid casts with colour-coded volumes indicated alongside. TolC is omitted for clarity.

Supplemental Tables

Table S1: Crystallographic data and refinement statistics for soluble domain structures of *E. coli* MacB

	Periplasmic domain	Cytoplasmic NBD (form I)	Cytoplasmic NBD (form II)
PDB code	5LJ8	5LJ9	5LJA
Data collection			
Beam line	DLS I24	DLS I24	DLS I24
Wavelength (Å)	0.96861	0.96861	0.96862
Crystal parameters			
Space group	$P2_1$	$P6_122$	$C222_1$
Unit cell dimensions (Å)	50.1, 54.9, 66.9	56.0, 56.0, 259.1	57.5, 96.2, 262.7
Unit cell angles (°)	90, 92.9, 90	90, 90, 120	90, 90, 90
Mosaic spread (°)	0.68	0.43	0.50
Reflection data *			
Resolution range (Å)	32.87-1.95 (2.00-1.95)	48.48-2.40 (2.49-2.40)	52.54-2.30 (2.38-2.30)
Unique reflections	26,585 (1,874)	10,332 (1,044)	31,381 (2,615)
R_{sym}	0.089 (0.542)	0.096 (0.820)	0.077 (0.431)
I/σ(I)	8.1 (1.9)	12.2 (1.8)	14.0 (4.9)
$CC_{½}$	0.99 (0.70)	1.00 (0.69)	0.998 (0.92)
Completeness (%)	99.8 (99.7)	100.0 (100.0)	95.2 (82.4)
Multiplicity	3.4 (3.2)	7.6 (4.9)	6.6 (6.3)
Wilson B ($Å^2$)	21.5	39.8	31.8
Refinement †			
Resolution (Å)	66.8 – 1.95	48.48 – 2.40	52.54-2.30
Number of reflections	25,260	9,759	29,723
R_{work}	0.178	0.223	0.186
R_{free}	0.228	0.297	0.225
Rms (bond lengths) (Å)	0.017	0.013	0.016
Rms (bond angles) (°)	1.66	1.73	1.73
Model composition			
Protein atoms	3,266	1,801	5,450
Waters	99	9	199
Model B-factors			
Protein atoms ($Å^2$)	25.8	56.1	39.4
Waters ($Å^2$)	29.4	48.9	36.6
Ramachandran statistics ‡			
Favoured (%)	99.0	97.4	97.9
Allowed (%)	0.8	2.6	2.1
Outliers (%)	0.3	0.0	0.0

* As reported by Aimless (19).
† As reported by Refmac (26).
‡ As reported by Rampage (28).
Values in parentheses indicate the outer resolution bin.

Table S2: Crystallographic data and refinement statistics for *A. actinomycetemcomitans* MacB

	Seleno-MacB Hexagonal	MacB Hexagonal	MacB Monoclinic I	MacB Monoclinic II
PDB code	-	5LJ6	5LIL	5LJ7
Data collection				
Beam line	DLS I24	DLS I24	Soleil PX2	DLS I24
Wavelength (Å)	0.91732	0.97943	0.9763	0.96861
Crystal parameters				
Space group	$P6_522$	$P6_522$	$P2_1$	$P2_1$
Unit cell dimensions (Å)	119.01, 119.01, 300.87	119.57, 199.57, 307.78	111.59, 82.62, 124.92	112.33, 82.61, 125.17
Unit cell angles (°)	90, 90, 120	90, 90, 120	90, 94.45, 90	90, 93.54, 90
Mosaic spread (°)	0.63	0.80	0.98	0.71
Number of crystals	1	1	3	1
Reflection data *				
Resolution range (Å)	60.17-5.00 [60.17-11.18] (5.59-5.00)	61.56-3.90 [61.56-8.72] (4.36-3.90)	79.95-3.35 [79.95-10.59] (3.53-3.35)	86.13-3.25 [86.13-11.26] (3.39-3.25)
Unique reflections	5,997 [635] (1,624)	12,392 [1,297] (3,286)	32,862 [1,110] (4,631)	36,201 [901] (4,429)
R_{sym}	0.145 [0.052] (1.792)	0.103 [0.051] (2.466)	0.284 [0.064] (1.522)	0.210 [0.071] (1.317)
R_{meas}	0.152 [0.057] (1.842)	0.108 [0.053] (2.585)	0.301 [0.069] (1.617)	0.230 [0.078] (1.436)
R_{pim}	0.028 [0.011] (0.324)	0.029 [0.015] (0.651)	0.099 [0.026] (0.541)	0.092 [0.033] (0.565)
I/σ(I)	16.1 [49.7] (3.1)	10.3 [36.5] (1.8)	7.7 [28.4] (2.1)	6.7 [17.6] (1.7)
CC½	1.00 (0.388)	0.997 (0.652)	0.993 (0.790)	0.995 (0.799)
Completeness (%)	100.0 [99.5] (100.0)	97.9 [99.8] (94.8)	99.6 [99.8] (97.1)	99.4 [96.6] (99.9)
Multiplicity	31.3 [26.2] (32.2)	13.8 (13.0)	9.3 (8.9)	6.1 (6.2)
Wilson B ($Å^2$)	291	215	125	38
Refinement †				
Resolution (Å)	-	59.79-3.90	79.95-3.35	86.13-3.25
Reflections	-	12,315	32,620	36,080
R_{work}	-	0.2675	0.2444	0.2447
R_{free}	-	0.3222	0.2902	0.2994
Rms (bond lengths) (Å)	-	0.004	0.003	0.003
Rms (bond angles) (°)	-	1.025	0.711	0.637
Model composition				
MacB	-	1	2	2
ATP	-	1	2	2
Mg^{2+}		1	2	2
Waters	-	-	4	4
Model B-factors				
MacB ($Å^2$)	-	239	100	103
ATP/Mg^{2+} ($Å^2$)	-	225	70	75
Waters ($Å^2$)	-	159	56	55
Ramachandran statistics ‡				
Favoured (%)	-	91.69	93.84	93.14
Allowed (%)	-	7.63	5.75	6.60
Outliers (%)	-	0.68	0.42	0.26

* As reported by Aimless (19).
† As reported by Refmac (26).
‡ As reported by Rampage (28).
Values in parentheses indicate the outer resolution bin.
Values in square brackets indicate the inner resolution bin..

Table S3: Antimicrobial susceptibility testing. MIC expressed as µg/mL.

Antimicrobial	Num. repeats		Mean±SD MIC		Median±SIQR MIC	
	WT	E170Q	WT	E170Q	WT	E170Q
Erythromycin (ERY)	24	24	31±3	1±0	32±8	1±0
Bacitracin (BAC)	24	24	8021±836	490±72	8192±0	512±0
Colistin (COL)	32	32	23±8	4±1	16±4	4±0
Kanamycin (KAN)	8	8	32±0	18±6	32±0	16±0
Chloramphenicol (CHL)	8	8	1±1	1±1	1±1	1±0
Ciprofloxacin (CIP)	8	8	1±0	1±0	1±0	1±0
Tetracycline (TET)	8	8	2±0	2±0	2±0	2±0
Gentamycin (GEN)	3	3	15±2	16±0	16±0	16±0
Sodium dodecyl sulphate (SDS)	8	8	>256	>256	>256	>256
Chlorhexidine (CHX)	8	8	2±0	2±1	2±1	2±0
Ethidium bromide (EBR)	8	8	2±0	2±0	2±0	2±0

Minimum Inhibitory Concentrations (MICs) expressed as µg/mL.

Mean±SD corresponds to the arithmetic mean ± standard deviation.

Median±SIQR corresponds to the median value ± semi-interquartile range.

Table S4: Erythromycin MIC data for wild type and variant MacB

Variant	Repeats	Mean±SD MIC	Median±SIQR MIC	Location	STII export
WT	32	40±15	32±4	-	+
Control	32	1±1	1±0.5	-	-
K47A	24	1±1	1±0.5	NBD	-
R121A	24	7±2	8±2	NBD	+
E170Q	24	1±0	1±0	NBD	-
E256A	24	24±14	16±8	Amphipathic helix	+
T275A	24	8±0	8±0	TM1	+
S285A	24	22±8	16±8	TM1	+
T311A	24	29±11	32±8	Porter I	+
D313A	24	21±8	16±8	Porter I	+
Y315A	24	6±2	4±2	Porter I	+
K318A	24	14±5	16±4	Porter I	+
D319A	24	7±3	8±2	Porter I	+
F320A	24	3±1	4±1	Porter I	+
D322A	24	13±4	16±4	Porter I	+
D323A	24	11±4	8±4	Porter I	+
D324A	24	19±10	16±12	Porter I	+
Q326A	24	32±0	32±0	Porter I	+
Y327A	24	16±8	16±4	Porter I	+
Q328A	24	32±0	32±0	Porter I	+
Q329A	24	28±7	32±2	Porter I	+
N335A	24	33±7	32±0	Porter I	+
T349A	24	2±1	2±0	Porter I	+
S353A	24	22±8	16±8	Sabre	+
N355A	24	21±8	16±8	Sabre	+
R357A	24	11±4	8±4	Sabre	+
R359A	24	13±4	16±4	Sabre	+
N361A	24	27±7	32±8	Sabre	+
N362A	24	28±11	32±8	Sabre	+
D364A	24	22±8	16±8	Sabre	+
S368A	24	14±4	16±1	Sabre	+
N370A	24	27±8	32±8	Sabre	+
V372A	24	15±6	16±1	Sabre	+
Y376A	24	1±0	1±0	Sabre	+
D405A	24	21±8	16±8	Sabre	+
S406A	24	27±8	32±8	Sabre	+
N407A	24	13±4	16±4	Sabre	+
R409A	24	27±8	32±8	Sabre	+
R410A	24	14±4	16±4	Sabre	+
Q411A	24	43±22	48±24	Sabre	+
N428E	24	84±32	64±32	Sabre	+
E438A	24	43±15	32±16	Sabre	+
E439A	24	41±17	32±16	Sabre	+

K440A	24	8±6	8±2	Sabre	+
Q441A	24	27±8	32±8	Sabre	+
S442A	24	9±3	8±0	Sabre	+
M443A	24	7±3	8±2	Sabre	+
F444A	24	2±1	2±0.5	Sabre	+
S446A	24	21±7	16±8	Sabre	+
S447A	24	8±2	8±0	Sabre	+
K448A	24	32±0	32±0	Sabre	+
R451A	24	9±3	8±0	Sabre	+
W453A	24	32±16	32±8	Sabre	+
Y456A	24	26±8	32±8	Sabre	+
R462E	24	43±15	32±16	Sabre	+
S471A	24	11±4	8±4	Porter II	+
T473A	24	21±8	16±8	Porter II	+
E486A	24	7±6	4±2	Porter II	+
H497A	24	32±23	32±8	Porter II	+
K499A	24	27±8	32±8	Porter II	+
K500A	24	52±16	64±16	Porter II	+
D501A	24	21±8	16±8	Porter II	+
F503A	24	4±1	4±0	Porter II	+
W505A	24	2±1	2±0	Porter II	+
M507A	24	3±1	3±1	Porter II	+
T517A	24	87±33	64±32	Stalk	+
T520A	24	64±46	32±48	Stalk	+
S532A	24	30±15	32±8	TM2	+
N542A	24	32±0	32±0	TM2	+
D322A+D323A+D324A	24	4±1	4±0	Porter	+
Y376A+F444A	24	1±0	1±0	Sabre	+
E438A+E439A	24	43±15	32±16	Sabre	+
Δ C-terminus	24	8±4	8±2	Minor coupling helix	+

Minimum Inhibitory Concentrations (MICs) expressed as µg/mL.

Mean±SD corresponds to the arithmetic mean ± standard deviation.

Median±SIQR corresponds to the median value ± semi-interquartile range.

The MacB periplasmic domain is made up of both Porter and Sabre subdomains. The Porter itself is formed from two discontinuous regions of primary sequence labelled here as Porter I and Porter II.

Abbreviations used: NBD, Nucleotide binding domain; TM1 and TM2, transmembrane helix 1 and transmembrane helix 2.

Table S5: Bacitracin and Colistin MIC data for MacB variants.

	Bacitracin			Colistin			
Variant	**N**	**Mean±SD**	**Median±SIQR**	**N**	**Mean±SD**	**Median±SIQR**	**Location**
WT	24	4096±0	4096±0	24	16±0	16±0	-
Control	24	277±72	256±0	24	6±2	4±2	-
K47A	24	256±0	256±0	24	6±2	4±2	NBD
E170Q	24	251±26	256±0	24	5±2	4±2	NBD
D313A	24	4096±0	4096±0	24	8±2	8±0	Porter I
T349A	24	2048±0	2048±0	24	10±5	8±6	Porter I
N355A	24	4096±0	4096±0	24	18±11	16±12	Sabre
Y376A	24	331±118	256±0	24	6±2	8±2	Sabre
N407A	24	3413±986	4096±1024	24	11±4	8±4	Sabre
F444A	24	491±72	512±0	24	6±2	6±2	Sabre
W505A	24	1024±0	1024±0	24	7±2	8±2	Porter II
Y376A+ F444A	24	352±127	256±128	24	5±2	4±2	Sabre

Minimum Inhibitory Concentrations (MICs) expressed as μg/mL.

N = number of repeats.

Mean±SD corresponds to the arithmetic mean ± standard deviation.

Median±SIQR corresponds to the median value ± semi-interquartile range.

Table S6: Cysteine-locking experiment MIC data.

	-			+ $Cu(II)Cl_2$			+DTT		
Variant	**N**	**Mean ±SD**	**Median ±SIQR**	**N**	**Mean ±SD**	**Median ±SIQR**	**N**	**Mean ±SD**	**Median ±SIQR**
WT	24	43±15	32±16	24	32±0	32±0	24	43±15	32±16
E170Q	24	1±1	1±1	24	2±1	1±1	24	1±0	1±0
T517A	16	64±0	64±0	16	62±8	64±0	16	64±0	64±0
T517C	16	16±0	16±0	16	5±2	4±1	16	46±21	64±18

Minimum Inhibitory Concentrations (MICs) for erythromycin expressed as µg/mL.

N = number of repeats.

Mean±SD corresponds to the arithmetic mean ± standard deviation.

Median±SIQR corresponds to the median value ± semi-interquartile range.

Table S7: Crystallographic data and refinement statistics for the periplasmic domain of *E. coli* LolC

	Periplasmic domain of *E. coli* LolC
PDB code	5NAA
Data collection	
Beam line	I03
Wavelength (Å)	0.9763
Crystal parameters	
Space group	C2
Unit cell dimensions (Å)	54.7, 111.8, 75.9
Unit cell angles (°)	90, 109, 90
Mosaic spread (°)	0.84
Reflection data *	
Resolution range (Å)	45.99-1.88 (1.92-1.88)
Unique reflections	34,822 (2,179)
R_{sym}	0.078 (0.436)
I/σ(I)	11.0 (2.4)
CC½	0.996 (0.759)
Completeness (%)	99.5 (98.1)
Multiplicity	5.1 (3.9)
Wilson B ($Å^2$)	24.8
Refinement †	
Resolution (Å)	45.99 (1.88)
Number of reflections	32,931
R_{work}	0.1798
R_{free}	0.2252
Rms (bond lengths) (Å)	0.018
Rms (bond angles) (°)	1.81
Model composition	
Protein atoms	3,467
Waters	240
Other	5
Model B-factors	
Protein atoms ($Å^2$)	32.9
Waters ($Å^2$)	37.0
Other	60.2
Ramachandran statistics ‡	
Favoured (%)	98.4
Allowed (%)	1.6
Outliers (%)	0.0

* As reported by Aimless(19).
† As reported by Refmac (26).
‡ As reported by Rampage (28).
Values in parentheses indicate the outer resolution bin.

Supplementary Methods

Construction of strains and plasmids

pET28-EcMacB, encoding N-terminally His-tagged *E. coli* MacB, was created by PCR amplification of *macB* from *E. coli* MG1655 genomic DNA, digestion with NdeI and BamHI, and ligation into pET28 (Novagen) digested with the same enzymes. MacB homologues from *A. actinomycetemcomitans, A. pleuropneumoniae, P. aeruginosa, P. syringae, R. capsulatus, S. marcescens, S. typhimurium* and *P. mirabilis* were cloned with a similar strategy. *A. actinomycetemcomitans* E169Q and *E. coli* E170Q MacB mutants were introduced by Quikchange site-directed mutagenesis. Plasmids expressing the *E. coli* MacB NBD (pMacB-NBD; residues 1-223) and the periplasmic domain (pMacB-Peri; residues 309-508) with C-terminal His-tags were created by PCR amplification of *E. coli* MG1655 genomic DNA, digestion of PCR products with NdeI and XhoI, and ligation into pET21a digested with the same enzymes. *E. coli macA* was cloned NdeI-XhoI into the second multiple cloning site (MCS) of pETDuet1 (Novagen) resulting in pDuet-MacA. For co-expression of *E. coli* MacAB, wild type *macB* was cloned NcoI-HindIII into the first MCS of pET-MacA resulting in pETDuet-MacAB. Point mutants were introduced into pETDuet-MacAB by Quikchange site-directed mutagenesis. Heat stable enterotoxin was amplified from pET11-STII (11) and cloned into pCDFDuet using NcoI and KpnI restriction sites resulting in pCDF-STII. The *E. coli* LolC periplasmic domain predicted by Octopus (12) (residues 48-266) was amplified from *E. coli* MG1655 genomic DNA, digested with NdeI and NotI and ligated into pET24 digested with the same enzymes resulting in pET24-EcperLolC. All clones were verified by DNA sequencing (Source Bioscience). The *macAB* locus in *E. coli* C43 (DE3) (13) was replaced with a kanamycin resistance cassette using the λ Red recombinase system (14). The resistance cassette was subsequently removed by transformation with plasmid pCP20 encoding the FLP recombinase (15) resulting in strain C43 (DE3) Δ*macAB*. Strain C43 (DE3) Δ*acrAB* Δ*macAB* was created by subsequent removal of *acrAB* in the same manner. Both deletions were confirmed by PCR of the gene locus.

Enterotoxin secretion assay

C43 (DE3) or C43 (DE3) Δ*macAB* bearing pCDF-STII and plasmid-borne *mac* genes as indicated were grown in 2YT medium at 37 °C until an OD_{600} of 0.4 was achieved. Protein production was induced with 0.5 mM IPTG and cultures grown for a further 2 hours. Cells were removed by centrifugation at 4000 *g* and the supernatant passed through a 0.22 μm filter. Supernatant samples (1 mL) were precipitated with 10 % trichloroacetic acid (final concentration), washed with acetone and then resuspended in SDS-PAGE loading buffer before analysis by SDS-PAGE on 10 % Bis-Tris gels. Identity of STII enterotoxin was confirmed by mass spectrometry (PNAC, University of Cambridge).

Minimum inhibitory concentration (MIC) determinations

C43 (DE3) Δ*acrAB* Δ*macAB* bearing pETDuet MacAB wild type or variant were induced with 0.2 mM IPTG for 1 hour before addition to wells of a 96 well plates containing 0.2 mM IPTG, 100 µg/ml carbenicillin and 2-fold serial dilution of the indicated drug in LB medium (final volume 180 µl per well). Dilutions were from a 1024 µg/ml stock for ethidium bromide, chlorhexidine, SDS, gentamycin, tetracycline, ciprofloxacin, kanamycin, colistin, erythromycin, 8192 µg/ml for bacitracin and 512 µg/ml for chloramphenicol. For disulfide crosslinking experiments, 0.2mM $CuCl_2$ or 2mM DTT were added as indicated. MICs were assessed after 16 hours growth at 30 ºC. Experiments were repeated at least 3 times.

Purification of full-length *A. actinomycetemcomitans* MacB

E. coli C43 (DE3) transformed with pET28-*Aa*MacB was grown in 2YT medium at 30 °C. At OD_{600} 0.5, the temperature was reduced to 18 °C and protein expression induced by addition of 0.4 mM IPTG. After 16 hours further growth, cells were harvested by centrifugation (6000 *g*) and the cell pellets resuspended in 50 mM HEPES pH 7.5, 200 mM NaCl supplemented with protease inhibitor cocktail (Roche) and broken by 2 passages through a Constant Systems cell disruptor at 30000 psi. Unbroken cells and debris were removed by centrifugation (10 mins, 18000 g) before membranes were collected by centrifugation at 150000 *g* for 1 hour at 4 °C. Membranes were resuspended in 25 mM HEPES pH 7.5, 150 mM NaCl, 10 % (v/v) glycerol supplemented with protease inhibitors and solubilised by addition of lauryl maltose neopentyl glycol (LMNG; 1 % (w/v) final concentration). Insoluble material was removed by centrifugation (45 mins, 150000 *g*) and the solubilised membranes added to IMAC resin (Biorad Profinity). The resin was washed with 25 mM HEPES pH 7.5, 500 mM NaCl, 0.03 % LMNG, 10 mM imidazole and eluted with 25 mM HEPES pH 7.5, 500 mM NaCl, 0.03 % LMNG, 250 mM imidazole. Protein was buffer exchanged into 25 mM HEPES pH 7.5, 150 mM NaCl, 0.02 % LMNG and concentrated using Amicon Ultra 15 centrifugal concentrators (100 kDa cut-off). Selenomethionine incorporated *Aa*MacB was produced using a metabolic inhibition protocol (16). C43 (DE3) cells bearing pET28-*Aa*MacB plasmid were grown at 37 °C to OD_{600} 0.5 in M9 minimal media supplemented with 50 µg/mL kanamycin, 0.2 % (w/v) glucose, 2 mM $MgSO_4$, 0.1 mM $CaCl_2$ and 0.001 % (w/v) thiamine. 100 mg/L of threonine, lysine and phenylalanine, 50 mg/L of leucine, isoleucine and valine and 60 mg/L of selenomethionine were added and cells grown for a further 45 minutes. Protein expression was induced with 0.5 mM IPTG and the cells grown for a further 16h at 18 °C. Selenomethionine labelled protein was purified as native with the addition of 1 mM TCEP to all buffers. Incorporation of selenomethionine residues was confirmed by mass-spectrometry.

Purification of MacB periplasmic and cytoplasmic domains

E. coli C43 (DE3) cultures bearing pMacB-NBD or pMacB-Peri were grown at 37 °C on 2YT media supplemented with 50 μg/mL carbenicillin. Protein expression was induced with 1 mM IPTG at an OD_{600} ~0.6 and the temperature reduced to 18 °C. After 16 hours further growth, cells were harvested by centrifugation and the pellets frozen at -80 °C. Thawed cell pellets were resuspended in IMAC wash buffer (50 mM HEPES pH 7.5, 300 mM NaCl, 25 mM imidazole), and lysed by passage through a Constant Systems Cell Disruptor (30200 psi). Lysate was centrifuged at 30000 *g* for 30 min at 6 °C to remove cellular debris and the supernatant loaded onto an immobilised Ni-affinity column pre-equilibrated with the wash buffer (25 mM HEPES pH 7.5, 300 mM NaCl, 25 mM imidazole). Bound proteins were washed with 15 column volumes of wash buffer before elution in 50 mM HEPES pH 7.5, 300 mM NaCl, 300 mM imidazole. Protein samples were exchanged into 20 mM HEPES pH 7.2, 150 mM NaCl and concentrated to ~10 mg/mL using a centrifugal filter (Amicon 10 kDa nominal molecular weight cut-off) and frozen in liquid nitrogen before storage at -80 °C.

Purification of *E. coli* LolC periplasmic domain

BL21 (DE3) cells bearing plasmid pET24-EcperLolC were grown in 1L of 2YT medium supplemented with 50 μg/mL of kanamycin at 30°C. When the culture had achieved OD_{600} of 0.8 the temperature was reduced to 18 °C and protein expression induced with 0.1 mM IPTG. After 16 h further growth, cells were harvested by centrifugation at 4000 *g* and the pellet resuspended in 50 mL of 50 mM HEPES pH 7.5, 300 mM NaCl supplemented with protease inhibitor cocktail (Roche), lysozyme and DNAse. Bacteria were lysed by cell disruption (Constant Systems) at 30200 psi before removal of bacteria debris by ultracentrifugation (40 mins, 115000 g at 5 °C). The supernatant was incubated with Ni-NTA agarose resin (Qiagen) for 1h, washed with 20 mL of 20 mM HEPES pH 7.5, 300 mM NaCl, 20 mM imidazole and bound protein eluted with 10 mL of the same buffer supplemented with 250 mM imidazole. Eluted protein was exchanged into 20 mM HEPES pH 7.5, 150 mM NaCl using a 10 kDa cut-off centricon device (Amicon) and concentrated to 30 mg/mL, before flash freezing and storage at -80°C.

Crystallisation of full-length *A. actinomycetemcomitans* MacB, *E. coli* MacB periplasmic and cytoplasmic domains and *E. coli* LolC periplasmic domain

All crystallisation trials were conducted using the sitting drop vapour diffusion method in 2-drop MRC plates. Crystallisation drops were 1 μL in volume, composed of either 333 nL protein solution and 666 nL crystallisation reagent, or else 333 nL reagent and 666 nL protein, and were equilibrated over an 80 μL volume of the reagent alone. For *A. actinomycetemcomitans* MacB, protein aliquots (8 mg/mL) were thawed on ice and 5 mM MgATP or MgATPγS added immediately prior to crystallisation. Diffracting crystals were obtained in 100 mM Na-citrate pH 5.5, 21 % (v/v) PEG400 after 5 days and were harvested a few days later. Crystals of the selenomethionine derivative were

obtained in the same conditions. For cryoprotection, single crystals were transferred into a solution composed of 75 % (v/v) of the crystallisation reagent from the well reservoir and supplemented with 25 % (v/v) ethylene glycol and flash frozen in litholoops. Crystals of the MacB cytoplasmic domain were obtained using 2.8 M sodium formate, 100 mM sodium acetate pH 4.6. Crystals of the MacB periplasmic domain were first obtained as dense, non-diffracting needle clusters in 200 mM ammonium acetate, 30 % (v/v) glycerol ethoxylate, 100 mM MES pH 6.5. Subsequent streak seeding into a simple optimisation screen yielded thin near 2-dimensional plates in 35 % (v/v) glycerol ethoxylate, 100 mM sodium citrate pH 5.6. Further matrix-seeding into several different broad screens using these partially-optimised crushed-crystals yielded numerous conditions under which crystals grew. Data were collected from crystals grown from seeds in 30 % (v/v) pentaerythritol ethoxylate (15/4 EO/OH), 6 % (w/v) polyvinylpyrrolidone, 100 mM HEPES pH 7.5. For cryoprotection, single crystals were transferred into a solution composed of 75 % (v/v) of the crystallisation reagent from the well reservoir and 25 % (v/v) ethylene glycol before being flash frozen in litholoops. Crystallisation of the periplasmic domain of *E. coli* LolC was carried out by mixing 0.5 μL of protein at 10 mg/mL and 0.5 μL of reservoir solution composed of 0.2 M ammonium sulfate, 0.1 M sodium acetate at pH 4.6, 30% (w/v) of PEG 2000 MME. Crystals were grown at 15 °C by the sitting drop vapour diffusion method over a reservoir of 80 μL in MRC plates. The cryoprotection solution was composed of the reservoir solution supplemented with 25% (v/v) of glycerol before being flash frozen in nylon loops.

Structure determination – *E. coli* MacB periplasmic and cytoplasmic domains

X-ray data was collected at Diamond Light Source (UK) and structure solution used programmes from the CCP4 suite (17). Data were integrated with Imosflm (18), scaled with Aimless (19), and phased by molecular replacement using Phaser (20). The *E. coli* periplasmic domain was phased using a search model comprising the separated subdomains of the *A. actinomycetemcomitans* periplasmic domain (21) (PDB code 3FTJ). For the cytoplasmic domain, molecular replacement used the nucleotide binding domain (NBD) from MJ0796 (22) (PDB code 1L2T) as a search probe. To minimise phase bias, new phases were calculated using density modification implemented in Parrot (23) without recombination with the starting phases. Structural models were built with Buccaneer (24) using the density modified map as a starting point followed by cycles of model building and refinement using Coot (25) and Refmac (26). Non-crystallographic symmetry (NCS) restraints were used throughout refinement where possible. Validation was assisted with tools from Coot (25), Procheck (27), Rampage (28), and Molprobity (29). For the MacB cytoplasmic domain, two crystal forms were obtained – the first in space group $C222_1$ and another in space group $P6_122$. Statistics for crystallographic datasets and refined models pertaining to the MacB soluble domain structures are presented in **Table S2**. Coordinates and structure factors have been deposited with the protein

databank, accession codes **5LJA** (cytoplasmic form I), **5LJ9** (cytoplasmic form II) and **5LJ8** (periplasmic domain).

Structure determination – full-length *A. actinomycetemcomitans* MacB

Two datasets were collected at Soleil Proxima2 from a single crystal at distinct locations with a starting phi rotation 90° apart. A further dataset was collected at Diamond I24 on a second crystal isomorphous to the first. Each dataset was integrated and scaled using Imosflm (18) and Aimless (19). Radiation damage in each dataset was judged from the batch behaviour of overall statistics such as I/σ(I) and R_{merge} in the high-resolution bin. Data taken from the first part of each of all three datasets was merged and scaled using Aimless (19), and a high resolution cut-off chosen (3.35 Å) taking into account the I/σ(I), completeness and $CC_{½}$ in the outer resolution bin. Similar considerations were made for the $P6_522$ dataset.

The location of the cytoplasmic domain within the $P2_1$ cell was determined using molecular replacement with Phaser (20). A two-copy solution was found in space group $P2_1$ using the *E. coli* MacB cytoplasmic domain. After remodelling the *A. actinomycetemcomitans* sequence on the molecular replacement probe, further density was apparent in the asymmetric unit but was not easily interpreted. Searching the hexagonal data using the partially refined dimer from the $P2_1$ solution yielded a clear solution in space group $P6_522$ with a single molecule located beside the two-fold crystal symmetry axis. Inspection of the $P6_522$ density map revealed tubular density corresponding to the 4 transmembrane helices. The helices were modelled in Coot (25) as geometrically perfect polyalanine α-helices and this model transferred back to the $P2_1$ form. After a round of refinement with Refmac (26) (including jelly-body and NCS restraints), density modification protocols were employed with Parrot (23), DM and Resolve (30). The density-modified maps clarified the connectivity and directions of the transmembrane helices allowing these to be rebuilt and refined. Subsequent molecular replacement searches using the Sabre subdomain from the *A. actinomycetemcomitans* MacB periplasmic domain as a probe (keeping the cytoplasmic domain and polyalanine TM helices fixed) revealed the location of the Sabre subdomains. After phase calculation, the missing Porter domain was identified by manual inspection of the map. The Porter subdomains were manually placed in Coot (25) and refined using rigid body protocol in Refmac (26). Phases calculated during subsequent NCS-restrained maximum likelihood refinement of this model were used as a starting point for modification in Resolve (30) giving a map for use in model building. Once the majority of the protein main chain was built and the connectivity established, the $P2_1$-form polyalanine model was used to back-solve the $P6_522$ native and selenomethionine datasets by molecular replacement. Calculation of an anomalous scattering map using the selenomethionine dataset revealed locations of the Selenium positions informing the location of the methionines in the MacB polyalanine model. Returning to the $P2_1$ dataset, the model was updated with the methionine positions and

sequence assignments made where possible. Cycles of model building and maximum likelihood refinement were used to iteratively improve the model including additions of side chains. Non-crystallographic symmetry restraints were applied throughout. Inspection of the NBD revealed density for ATPγS, which was modelled as ATP and manually placed with assistance from real space fitting procedures in Coot (25). It was not possible to unambiguously identify the location of the oxygen-replacing sulfur in the ATPγS molecule. Near the end of refinement, validation tools from Coot (25), Molprobity (29), and Rampage (28) were used to guide further improvement of the model. In the final stages, refinement was switched from Refmac (26) to phenix.refine (31, 32). More than 120 iterative rounds of modelling and refinement were used to complete the model of MacB in space group $P2_1$. The final model of the $P2_1$ crystal form includes two MacB monomers, two ATP molecules, two magnesium ions and 4 crystallographically ordered waters. Residues 240-245, 312-324, 437-444 were not sufficiently well-resolved to model.

The structure of the $P6_522$ MacB crystal form was solved using the 3.35 Å structure of the $P2_1$ form as a starting model. Since the location of the NBD in the $P6_522$ cell was already known, a single monomer of the $P2_1$-form MacB structure was superposed using SSM (33) and subjected to rigid body refinement against the $P6_522$ data. This served as an initial model for the $P6_522$ form, which was then further improved by multiple iterations of model editing with Coot (25) and refinement with phenix.refine (31) using the $P2_1$ structure as a reference model. As refinement neared convergence, reference model restraints were released giving improvements in both R_{work} and R_{free}. Validation used tools from Coot (25), Procheck (27) and Rampage (28).

A final MacB structure was solved at 3.25 Å by refining the $P2_1$ form against data collected from a single crystal that was co-crystallised with regular ATP. No significant differences were observed, but the most complete model was derived from the 3.35 Å data. PDB accession codes for the full-length *A. actinomycetemcomitans* MacB are **5LIL** and **5LJ7** for the 3.35 Å and 3.25 Å monoclinic ($P2_1$) form and **5LJ6** for the hexagonal ($P6_522$) form.

Analysis of protein structures were assisted by various programs; the Dali server (34) was used for comparison with known structures, SSM superpose (33) for structural superpositions, ClustalOmega (35) for multiple sequence alignments. Positioning of MacB within the lipid bilayer was predicted using MEMEMBED (36). Analysis and visualisation of cavities within proteins was performed with POREWALKER (9) and HOLLOW (8). The homology model of *E. coli* MacB in the ATP bound state was constructed in I-TASSER (37) based on the full length *A. actinomycetemcomitans* MacB with assistance from our structures of the *E. coli* NBD (**5LJA**, **5LJ9** and periplasmic domains (**5LJ8)**. Structure images and movies were produced with PyMOL (38).

Structure determination – *E. coli* LolC periplasmic domain

Data were collected under cryogenic conditions at beamline I03 at Diamond Light Source (UK). The structure was refined with the CCP4 package (17). Images were integrated with Imosflm (18) and scaled with Aimless (19). The structure was solved by molecular replacement with Phaser (20) using the periplasmic domain of *A. actinomycetemcomitans* MacB (PDB 5LIL) as search model, but conserving only the β-sheet of the Porter subdomain. Electron density was improved with Parrot (23) before building the model with Buccaneer (24) and several rounds of manual refinement using Coot (25) and Refmac (26) with NCS restraints. Data collection and refinement statistics are shown in **Table S7.**

Supplementary References

1. Hollenstein K, Frei DC, Locher KP (2007) Structure of an ABC transporter in complex with its binding protein. *Nature* 446(7132):213–216.
2. Korkhov VM, Mireku SA., Locher KP (2012) Structure of AMP-PNP-bound vitamin B12 transporter BtuCD–F. *Nature* 490(7420):367–372.
3. Xu K, et al. (2013) Crystal structure of a folate energy-coupling factor transporter from *Lactobacillus brevis*. *Nature* 497(7448):268–71.
4. Dawson RJP, Locher KP (2006) Structure of a bacterial multidrug ABC transporter. *Nature* 443(7108):180–185.
5. Lee J-Y, et al. (2016) Crystal structure of the human sterol transporter ABCG5/ABCG8. *Nature*:1–17.
6. Luo Q, et al. (2017) Structural basis for lipopolysaccharide extraction by ABC transporter $LptB_2FG$. *Nat Struct Mol Biol* 24(5):469–474.
7. ter Beek J, Guskov A, Slotboom DJ (2014) Structural diversity of ABC transporters. *J Gen Physiol* 143(4):419–435.
8. Ho BK, Gruswitz F (2008) HOLLOW: generating accurate representations of channel and interior surfaces in molecular structures. *BMC Struct Biol* 8(1):49.
9. Pellegrini-Calace M, Maiwald T, Thornton JM (2009) PoreWalker: A novel tool for the identification and characterization of channels in transmembrane proteins from their three-dimensional structure. *PLoS Comput Biol* 5(7).
10. Krissinel E, Henrick K (2007) Inference of macromolecular assemblies from crystalline state. *J Mol Biol* 372(3):774–97.
11. Yamanaka H, Kobayashi H, Takahashi E, Okamoto K (2008) MacAB is involved in the secretion of *Escherichia coli* heat-stable enterotoxin II. *J Bacteriol* 190(23):7693–7698.
12. Viklund H, Elofsson A (2008) OCTOPUS: improving topology prediction by two-track ANN-based preference scores and an extended topological grammar. *Bioinformatics* 24(15):1662–1668.
13. Miroux B, Walker JE (1996) Over-production of Proteins in *Escherichia coli*: Mutant Hosts that Allow Synthesis of some Membrane Proteins and Globular Proteins at High Levels. *J Mol Biol* 260(3):289–298.
14. Datsenko KA, Wanner BL (2000) One-step inactivation of chromosomal genes in *Escherichia coli* K-12 using PCR products. *Proc Natl Acad Sci U S A* 97(12):6640–5.
15. Cherepanov PP, Wackernagel W (1995) Gene disruption in *Escherichia coli*: TcR and KmR cassettes with the option of Flp-catalyzed excision of the antibiotic-resistance determinant. *Gene* 158(1):9–14.

16. Van Duyne GD, Standaert RF, Karplus PA, Schreiber SL, Clardy J (1993) Atomic Structures of the Human Immunophilin FKBP-12 Complexes with FK506 and Rapamycin. *J Mol Biol* 229(1):105–124.
17. Winn MD, et al. (2011) Overview of the CCP4 suite and current developments. *Acta Crystallogr Sect D Biol Crystallogr* 67:235–242.
18. Battye TGG, Kontogiannis L, Johnson O, Powell HR, Leslie AGW (2011) iMOSFLM: A new graphical interface for diffraction-image processing with MOSFLM. *Acta Crystallogr Sect D Biol Crystallogr* 67:271–281.
19. Evans PR, Murshudov GN (2013) How good are my data and what is the resolution? *Acta Crystallogr Sect D Biol Crystallogr* 69(7):1204–1214.
20. McCoy AJ, et al. (2007) Phaser crystallographic software. *J Appl Crystallogr* 40:658–674.
21. Xu Y, et al. (2009) Crystal structure of the periplasmic region of MacB, a noncanonic ABC transporter. *Biochemistry* 48(23):5218–5225.
22. Smith PC, et al. (2002) ATP binding to the motor domain from an ABC transporter drives formation of a nucleotide sandwich dimer. *Mol Cell* 10(1):139–149.
23. Cowtan K (2010) Recent developments in classical density modification. *Acta Crystallogr Sect D Biol Crystallogr* 66:470–478.
24. Cowtan K (2006) The Buccaneer software for automated model building. 1. Tracing protein chains. *Acta Crystallogr Sect D Biol Crystallogr* 62:1002–1011.
25. Emsley P, Lohkamp B, Scott WG, Cowtan K (2010) Features and development of Coot. *Acta Crystallogr Sect D Biol Crystallogr* 66:486–501.
26. Murshudov GN, et al. (2011) REFMAC5 for the refinement of macromolecular crystal structures. *Acta Crystallogr Sect D Biol Crystallogr* 67:355–367.
27. Laskowski RA., MacArthur MW, Moss DS, Thornton JM (1993) PROCHECK: a program to check the stereochemical quality of protein structures. *J Appl Crystallogr* 26(2):283–291.
28. Lovell SC, et al. (2003) Structure validation by C alpha geometry: phi,psi and C beta deviation. *Proteins-Structure Funct Genet* 50(3):437–450.
29. Chen VB, et al. (2010) MolProbity: All-atom structure validation for macromolecular crystallography. *Acta Crystallogr Sect D Biol Crystallogr* 66:12–21.
30. Terwilliger TC (2003) research papers Statistical density modification using local pattern matching research papers. *Acta Crystallogr Sect D*:1688–1701.
31. Afonine P V., et al. (2012) Towards automated crystallographic structure refinement with phenix.refine. *Acta Crystallogr Sect D Biol Crystallogr* 68(4):352–367.
32. Adams PD, et al. (2002) PHENIX: Building new software for automated crystallographic structure determination. *Acta Crystallogr Sect D Biol Crystallogr* 58(11):1948–1954.
33. Krissinel E, Henrick K (2004) Secondary-structure matching (SSM), a new tool for fast protein structure alignment in three dimensions. *Acta Crystallogr Sect D Biol Crystallogr* 60(12

I):2256–2268.

34. Holm L, Rosenström P (2010) Dali server: Conservation mapping in 3D. *Nucleic Acids Res* 38(2):545–549.
35. Sievers F, et al. (2011) Fast, scalable generation of high-quality protein multiple sequence alignments using Clustal Omega. *Mol Syst Biol* 7(1):539.
36. Nugent T, Jones DT (2013) Membrane protein orientation and refinement using a knowledge-based statistical potential. *BMC Bioinformatics* 14(1):276.
37. Yang J, et al. (2014) The I-TASSER Suite: protein structure and function prediction. *Nat Methods* 12(1):7–8.
38. DeLano WL (2002) The PyMOL Molecular Graphics System. *Schrödinger LLC* http://www.pymol.org